Title

Buckling instability underlies vertebral segmentation during axolotl tail regeneration

Authors

Wouter Masselink[1,2,*], Tobias Gerber[3,4], Vijayishwer Singh Jamwal[5,6], Francisco Falcon[1,2,7], Tom Deshayes[1,8], Riley Grindle[5], Ryan P. Seaman[5], Marco Röcklinger[9], Sofia-Christina Papadopoulos[5,10], Gisela Deneke[1], Adrija Adhikary[1], Orestis G. Andriotis[9], Marko Pende[5], Yuka Taniguchi-Sugiura[1], Tzi-Yang Lin[1,7], Thomas Kurth[11], Jingkui Wang[1,2], Detlev Arendt[4], Ji-Feng Fei[12], Barbara Treutlein[3, 13], Fred W. Kolling[14], Philipp J. Thurner[9], Joel H. Graber[5], Edouard Hannezo[15], Elly M. Tanaka[1,2,*], Prayag Murawala[1,5,10,*]

1. Research Institute of Molecular Pathology (IMP), Vienna BioCenter (VBC), 1030 Vienna Austria.
2. Institute of Molecular Biotechnology of the Austrian Academy of Sciences (IMBA), Vienna BioCenter (VBC), 1030 Vienna.
3. Max Planck Institute for Evolutionary Anthropology, 04103 Leipzig, Germany.
4. European Molecular Biology Laboratory (EMBL), Developmental Biology Unit, 69117 Heidelberg, Germany.
5. MDI Biological Laboratory (MDIBL), Bar Harbor, ME 04609, USA.
6. Department of Molecular & Biomedical Sciences, University of Maine, Orono, ME 04469, USA.
7. Vienna BioCenter PhD Program, Doctoral School of the University of Vienna and Medical University of Vienna, 1030 Vienna, Austria.
8. École Normale Supérieure de Lyon, Université Claude Bernard Lyon 1, Université de Lyon, 69342 Lyon, France.
9. Institute of Lightweight Design and Structural Biomechanics, TU Wien, 1060, Vienna, Austria.

10. Department of Nephrology and Hypertension, Hannover Medical School, 30625 Hannover, Germany.

11. Core Facility Electron Microscopy and Histology. Center for Molecular and Cellular Bioengineering (CMCB), Technology Platform, Technische Universität Dresden, 01307, Dresden, Germany.

12. Department of Pathology, Guangdong Provincial People's Hospital (Guangdong Academy of Medical Sciences), Southern Medical University, 510080 Guangzhou, China

13. Department of Biosystems Science and Engineering, ETH Zurich, Basel 4058, Switzerland.

14. Dartmouth Cancer Center, Dartmouth Geisel School of Medicine, Lebanon, New Hampshire, USA

15. Institute of Science and Technology Austria, Am Campus 1, 3400 Klosterneuburg, Austria

* Correspondence: wouter.masselink@imba.oeaw.ac.at, elly.tanaka@imba.oeaw.ac.at, pmurawala@mdibl.org

Abstract

Primary body-axis development is a highly conserved process that proceeds through somitogenesis and subsequent subdivision into dermatome, myotome, and sclerotome. Defects in somitic-clock genes such as *Hes7* lead to vertebral-segmentation defects in mice and fish. Here we show that in the axolotl, although *Hes7* is necessary for proper embryonic vertebral segmentation, it is—surprisingly—dispensable during tail regeneration. We investigated the mechanism of vertebral segmentation during regeneration which initially occurs through extension of a cartilage rod ventral to the spinal cord. We find that the regenerating cartilage rod undergoes a periodic wrinkling that provides a template for vertebral segmentation. Via direct mechanical measurements and biophysical perturbations, we show that a model of compression-induced buckling instability can predict vertebral segmentation. The cartilage rod and other somitic derivatives (muscle, cartilage, tendon, fibroblasts) arise from tendon-like, *Lfng*$^{+}$ multi-potent mesenchymal progenitors, which display a gene regulatory state distinct from somitic progenitors. In summary, we uncover a mechanism of vertebral segmentation during axolotl tail regeneration that is distinct from the somite-based developmental mechanism.

52 **Main text**

53 Regeneration of the axolotl tail, which is composed of a spinal cord surrounded by
54 segmented vertebrae and muscle, is a rare example of primary body-axis regeneration among
55 vertebrates. While the cellular and molecular basis of spinal-cord regeneration in axolotl has been
56 characterized[1,2], very little is known about how somitic derivatives such as vertebrae are
57 regenerated in axolotl. In vertebrate animals, embryonic development and regeneration have
58 similar outcomes, but their starting points differ, and the question of when the pathways underlying
59 regeneration converge with those underlying development has fascinated generations of
60 researchers[3]. Beyond the differences in starting points, patterning during regeneration of post-
61 embryonic structures occurs at much larger spatial scales compared to embryonic patterning,
62 which suggests that different mechanisms could be at play. During vertebrate embryonic
63 development, patterning of the primary body axis is dependent on somitogenesis. Somites are
64 epithelial balls of cells on either side of the notochord and are specified through the clock-and-
65 wavefront model[4,5]. Somites contain multipotent progenitors that respond to cues from the
66 notochord and then lay out the architecture of the tail; these progenitors are the source of vertebrae
67 and myomeres in addition to other connective-tissue cell types[6,7]. In the axolotl, regeneration takes
68 place in the absence of the notochord and somites; instead, blastema cells condense into a cartilage
69 rod, after which vertebrae emerge[8]. In this study we asked: what is the cell source and mechanism
70 of vertebral patterning during regeneration?

71

72 **Hallmarks of somitogenesis are absent during tail regeneration**

73 We investigated two hallmarks of vertebral segmentation during embryogenesis and
74 regeneration, i.e., the formation of epithelial somites, and their subsequent resegmentation. During

75 embryogenesis in axolotls and other vertebrates, the tail contains histologically distinct somites
76 that give rise to vertebrae, muscles, and other types of connective-tissue cells. We found that during
77 regeneration of the axolotl tail, the tail blastema does not contain histologically distinct somites,
78 in contrast to embryogenesis (Fig. 1a, b, Extended Data Fig. 1a). Instead, the earliest visibly
79 segmented structures during regeneration are myomeres which appear around 14 days post
80 amputation (dpa) (Fig.1b, Extended Data Fig. 1a). Nevertheless, despite the absence of somites,
81 both the number of myomeres and vertebrae are correctly re-established in the axolotl tail (Fig.
82 1c-e) (uninjured: 20.10 +/- 1.45 vs regenerated 19.20 +/- 2.10) [9]. Axolotl embryos, similar to many
83 other vertebrates, undergo resegmentation, where rostro-caudal specification of somites into
84 *Uncx*$^{+}$ and *Tbx18*$^{+}$ domains results in a half-segment off-set between myomeres and vertebrae
85 (Fig. 1f-h)[10–12]. Consistent with our observation of a histological absence of somites during
86 regeneration (Fig. 1b, Extended Data Fig. 1a), we found that somite-dependent resegmentation is
87 also absent during regeneration (Fig. 1i-l).

88 To understand the processes underlying re-establishment of periodic segments during
89 axolotl tail regeneration, we performed Xenium spatial transcriptomics (Fig. 2a) on stage-28
90 embryos and on tail blastemas at 3, 7, 10, and 14 dpa (Fig. 2b-e, Extended Data Fig. 1b-i, 2). We
91 selected 100 target genes to visualize not only cell and lineage identity but also pathways known
92 to participate in tissue patterning and signaling, including distal HOX genes, and the FGF, Notch,
93 retinoic acid (RA), Wnt, BMP, and SHH signaling pathways (Extended Data Table 1). Using
94 Xenium clustering analysis, we identified eight cell types in embryo and eight in tail blastema (Fig.
95 2c, e, Extended Data Fig. 2a, h, o).We found that both embryos and blastemas express distal HOX
96 genes, *Fgfr1*, *Wnt5a,* and the Wnt/B-cat downstream target *Aldh1a2*, as well as the cell identity
97 markers *Scx, Lfng,* and *Meox1*(Extended Data Fig. 1b-i, 2c-e, j-l, q-s). While *Hes7*, *Tbx6*, and

98 *Mesp2* expression was present in the embryonic tail bud, it was absent in the tail blastema (Fig. 2f,
99 g, Extended Data Fig. 2f, m, t).

100 In axolotl embryos, we observed polarized somitic expression of resegmentation markers
101 *Tbx18* and *Uncx4.1*, but neither was expressed in the tail blastema (Extended Data Fig. 1d-e, 2g,
102 n, u). Hematoxylin and eosin (H&E) staining and the absence of *Tbx18/Uncx4.1* rostro-caudal
103 polarity strongly argue against classic epithelial somites at blastema stages. Together, these results
104 show that while the tail bud and tail blastema exhibit some similarities in their expression of genes
105 associated with *Fgf*, *Wnt*, and RA signaling, we did not detect somite like epithelial units in the
106 blastema via H&E staining.

107

108 **Hes7 is dispensable for vertebral segmentation during regeneration**

109 To determine directly whether somitogenesis-dependent patterning takes place during
110 regeneration, we generated a somitic-clock mutant axolotl through targeted mutagenesis of *Hes7*.
111 The Hairy and enhancer of split (Hes/Her) family of bHLH transcription factors is a family of
112 highly conserved oscillatory genes involved in somitogenesis, including *Hes7* (Extended Data Fig.
113 3a, b), which shows variable expression in the axolotl tail bud consistent with a role as a somitic
114 oscillator (Fig. 2f)[13]. *Hes7* mutant mice display aberrant somite-boundary formation, resulting in
115 vertebral-segmentation defects[14,15]. To generate *Hes7* mutant axolotls, we injected eggs with
116 Cas9/gRNA complexes representing a mixture of four gRNAs targeting all three exons of the *Hes7*
117 gene sequence (Extended Data Fig. 3b). We were unable to recover homozygous *Hes7* mutant
118 axolotls, as they are apparently embryonic lethal. We could, however, analyze mosaic F0 crispants,
119 which escaped embryonic lethality. We imaged vertebrae of F0 crispants using Alizarin Red S in
120 live, 4-5-cm-long animals. As in mice, these mutant axolotls displayed irregular vertebral

121 segmentation and fusions (Fig. 2h, i) consistent with a role for *Hes7* in somitogenesis during
122 embryonic development. Surprisingly these mutant tails recover a wildtype phenotype following
123 amputation, at which time the tails display regular vertebral segmentation and the normal number
124 of tail vertebrae (Fig. 2j-l, Extended Data Fig. 3c-e). To ensure that this observation did not result
125 from positive selection of wildtype and heterozygotic cells in the regenerate, we analyzed editing
126 efficiencies at each exonic target site in the unamputated tail close to the amputation plane and in
127 the regenerated tails. We found no significant difference in editing efficiency among the target
128 sites (Fig. 2m), indicating that, vertebral segmentation during axolotl tail regeneration proceeds
129 without a detectable requirement for *Hes7* under mosaic loss-of-function conditions. In summary,
130 we show that while vertebral segmentation takes place during tail regeneration, it does so through
131 a non-canonical somite-independent program.
132
133 **Somite-like lineage potential in the regenerating tail**
134 We next set out to identify the source of the newly regenerated musculo-skeletal tissues in
135 the axolotl tail. To survey the potency of cells that regenerate the tail, we performed clonal barcode
136 lineage tracing in the regenerated axolotl tail using a CellTag-based strategy adapted to a third-
137 generation foamy virus vector system[16–18]. We generated three unique libraries, each containing a
138 9-nt barcode and a defined 6-nt tag (V1, V2, V3) (Fig. 3a, Extended Data Fig. 4a-c) associated
139 with the 5' end of a GFP-encoding insert. High-titer viral libraries (Extended Data Fig. 4d) were
140 used to infect each tail four days prior to amputation (V1), as well as four (V2) and seven (V3)
141 dpa (Fig. 3b, c). We recovered V1, V2, and V3 barcodes from single-cell RNA-sequencing
142 (scRNA-seq) data of flow-sorted GFP^+ cells at 21 dpa (Fig. 3d-e, Extended Data Fig. 4e-h). To
143 identify putative clones, we calculated the Jaccard similarity index of barcodes detected in cells

144 with somite-derivative signatures (tenocytes, intermediate fibroblasts, dermis, fin mesenchyme,
145 chondrocytes, and myogenic cells) because of fate-mapping studies presented in the next section
146 (Fig. 3f). This analysis identified clones ranging in size from 2-6 cells, which suggests an
147 approximately 6-19% recovery rate when compared to an expected average clone size of 32.89
148 (V1), 16.91 (V2), and 10.27 (V3) cells, assuming a blastema cell-cycle length of 100 hours[9]. Of
149 the 48 clones analyzed, 39 contained diverse combinations of 2-4 cell types (Fig. 3f). Notably,
150 myogenic cells showed a clonal relationship with each of the other five cell types. Moreover,
151 computational mixing of the two replicates and subsequent clone-calling resulted in correct
152 annotation of 47 of 48 clones, indicating a sufficient diversity of barcodes (Extended Data Fig. 4h-
153 i). Although we did not recover any one clone containing all six cell types, these data are
154 compatible with a model in which a multipotent progenitor in the tail that has potential similar to
155 that of pre-somitic mesoderm, and that may give rise to Dermo-Myo-Sclerogenic (DMS) lineages
156 during regeneration (Extended Data Fig. 4j).
157

158 **Intermyotomal cells are the source of multipotent musculo-skeletal progenitors**

159 We next aimed to identify and characterize the origin and nature of these progenitors,
160 hypothesizing that they may arise at least in part from connective tissue. We first grafted vertebrae
161 from a constitutively expressing *CAGGs:GFP* transgenic axolotl into an unlabeled host axolotl
162 and observed minimal contribution from vertebrae cells (Extended Data Fig. 5a-d), eliminating
163 vertebrae as a cell source. We then performed Cre/*lox*P genetic fate mapping of tail regeneration
164 using two connective-tissue-specific *Cre-ERT2*-expressing drivers (*Col1A2* and *Twist3*) in
165 combination with a *CAGGs:LoxP-STOP-LoxP-Cherry* reporter, and inducing recombination 10
166 days prior to tail amputation. Prior to amputation, the *Col1A2* driver broadly labeled the tail

167 connective-tissue population (fin mesenchyme, dermal fibroblasts, tenocytes, and periskeletal and
168 skeletal cells) (Fig. 4a). The *Twist3* driver labeled a smaller subset of tail connective tissue
169 including fin mesenchyme, dermal fibroblasts, and skeletal lineage, but showed very limited
170 labeling of connective-tissue cells residing at the intermyotomal boundaries (Fig. 4b). After tail
171 amputation, the *Twist3* driver showed limited participation of the labeled cells to the regenerate
172 (Fig. 4d, f, Extended Data Fig. 5e-h). In contrast, the *Col1A2* driver contributed labeled cells to
173 regenerated fin mesenchyme, tenocytes, and vertebrae as well as muscle (Fig. 4c, e, Extended Data
174 Fig. 5e-h), consistent with the notion of a common source cell for connective-tissue and muscle
175 lineages. This further excludes dermal fibroblasts and fin mesenchymal cells as the likely cell
176 source and suggests tenocytes as the likely cells source. To assess whether muscle labeling is due
177 to non-specific labeling of the myogenic lineage, such as satellite cells, we performed sectioning
178 and immunostaining with the muscle-progenitor marker PAX7. In converted, unamputated tails
179 we observed no colocalization between Cherry^{+} cells and *PAX7*$^{+}$ muscle progenitors (Extended
180 Data Fig. 5i). However, regenerated tails showed the presence of Cherry^{+}/PAX7^{-}, Cherry^{-}/PAX7^{+},
181 and Cherry^{+}/PAX7^{+} populations in addition to Cherry^{+} muscle fibers, suggesting that *Col1A2*-
182 labeled Cherry+ cells give rise to at least some PAX7+ muscle progenitors (Extended Data Fig.
183 5j).

184 To molecularly pinpoint the potential source cells, we generated scRNAseq data of flow-
185 sorted cells from both the *Col1A2* and *Twist3* driver lines (Extended Data Fig. 6a) and annotated
186 six connective-tissue cell types (tenocytes, fibroblasts, chondrocytes, fin mesenchyme, dermis, and
187 periskeleton) and corroborated cell identities by HCR *in situ* hybridization (Extended Data Fig 6b-
188 h) to localize fin mesenchyme (*Prrx1*$^{+}$), dermal fibroblasts (*Prrx1*^{low}/*Twist3*$^{+}$), periskeletal cells
189 (*Chrdl1*$^{+}$), chondrocytes (*Sox9*$^{+}$), and tenocytes (*Scx*$^{+}$) at intermyotomal boundaries. Consistent

190 with tenocytes as the potential source cells we found tenocytes were depleted in our *Twist3* lineage
191 labelled populations. We found that genes expressed by tenocytes include *Lfng* and *Meox1*
192 *(*Extended Data Fig. 6b), which are also expressed during somitic mesoderm development
193 (Extended Data Fig. 1g), in addition to canonical tenocyte markers such as *Tnmd, Scx*, and *Mkx*
194 (Fig. 4i). Immunogold labeling of *Col1a2*-labeled cells identified Cherry+ cells between
195 myomeres that interact with muscle-fiber ends through collagen deposition (Extended Data Fig.
196 6i-j). Further, whole-body light-sheet imaging of *Col1A2* animals stained for PCNA (proliferative
197 cells) showed that Cherry^{+}/PCNA^{+} cells reside in the intermyotomal space in mature tails
198 (Extended Data Fig. 6k). Together, our results suggest that tenocytes labeled by *Scx, Meox,* or *Lfng*
199 are a source population for dermo-, myo-, and sclerogenic lineages respectively in the tail. In
200 addition, based on these results and those of the viral barcoding experiment, we hypothesize that
201 these tenocytes represent multipotent DMS-progenitors in the mature tail.

202 To assess the trajectories and molecular features by which DMS-progenitors differentiate
203 during tail regeneration, we performed scRNA-seq analysis on the *Col1A2*-labeled lineages at one
204 and two weeks post-amputation (wpa) (Fig. 4g). Consistent with our hypothesis, trajectory analysis
205 implicated tenocytes as DMS-progenitors (Fig. 4 h, j), and later blastema time points showed
206 emergence of the myogenic lineage in the *Col1A2* driver dataset (Fig. 4g'). The transcriptional
207 signatures of all blastema cell clusters were similar to those identified in the mature tail (Fig. 4k,
208 l). This suggests that no unique cell cluster emerges during regeneration, and that DMS-progenitors
209 represent a resident progenitor population of the mature tail. Using HCR-ISH of *Lfng*$^{+}$/*Meox1*$^{+}$ as
210 a marker for DMS-progenitors, we examined their localization during regeneration (Extended Data
211 Fig. 7a-f). At 1 wpa, we found accumulation of DMS-progenitors throughout the blastema

212 (Extended Data Fig. 7a-c), while at 2 wpa, myomeres separated by DMS-progenitors emerged
213 (Extended data Fig. 7d-f).

214 To test whether *Lfng*-expressing cells in the intermyotomal space indeed represent source
215 cells for regeneration, we generated an *Lfng*-driven Cre-ERT2-expressing transgenic axolotl line.
216 Conversion of the *Lfng* driver 10 days prior to regeneration showed that Cherry expression was
217 absent in the fin mesenchyme and was restricted to the inter-myotome population of the medial
218 axolotl tail (Fig. 4m). Upon tail amputation, the *Lfng* descendants contributed extensively to all
219 somitic mesodermal lineages of the regenerating tail (Fig. 4n, o, Extended Data Fig. 5e-h),
220 suggesting faithful labeling of DMS-progenitors. To examine whether *Lfng*-labeled DMS-
221 progenitors are necessary for tail regeneration, we crossed the *Lfng*-driven CreERT2-expressing
222 transgenic axolotl line to a *lox*P-dependent NTR2.0 (second-generation of nitroreductase)
223 transgenic line (*CAGGS:LoxP-nBFP-LoxP-Cherry-T2A-NTR2.0*[19]). Upon nifurpirinol treatment,
224 we found that ablation of *Lfng*-labeled DMS-progenitors prevented complete tail outgrowth (Fig.
225 4p-t). We did not quantify ablation efficiency or lineage selectively; therefore, incomplete or off-
226 target ablation effects cannot be fully excluded. Based on these results, together, we conclude that
227 *Lfng*$^{+}$ DMS-progenitors contribute to regeneration of somitic lineages and are required for
228 complete tail outgrowth in our ablation paradigm.

229

230 **DMS-progenitors represent a non-embryonic identity**

231 Our *Hes7*-mutant and scRNA-seq data suggest that regeneration of somitic mesoderm
232 lineages in axolotl differs from the embryonic program. This would contrast with regeneration of
233 limbs in axolotl, where limb connective-tissue cells dedifferentiate to a state that is molecularly
234 comparable to a limb-bud mesenchyme progenitor[20]. To further investigate this contrast in

235 processes, we integrated all mature and regeneration timepoints into a single UMAP (Extended
236 Data Figure 8a-c) and performed scRNAseq on four tail-bud stages (stage 25, 28, 30, 35). Results
237 showed that, consistent with our earlier Xenium spatial transcriptomic analysis, genes commonly
238 associated with somitogenesis and resegmentation were expressed during embryonic development
239 but did not show increased expression during tail regeneration compared to uninjured tails (Fig.
240 5a-b). However, we did detect expression of the DMS markers *Lfng* and *Meox1* in the combined
241 mature dataset (Fig. 5b). In addition, we observed expression of two highly conserved markers of
242 resegmentation (*Uncx4.1* and *Tbx18*) in the embryo via scRNAseq, Xenium spatial
243 transcriptomics, and HCR-ISH (Fig. 5b, Extended Data Fig. 1h, 8c, d), but neither technique
244 showed expression of these markers during tail regeneration (Fig. 5b, Extended Data Figure 1i,
245 2g, n, u 8c, e) Finally, to assess whether tail blastema cells acquire tail-bud-like identities, we
246 performed quadratic programing on published limb[21] and the above tail development and
247 regeneration datasets. Results show that unlike limb blastema cells which acquire a limb-bud
248 identity, tail blastema cells do not acquire a tail-bud identity (Fig. 5c). In summary, DMS-
249 progenitors have a distinct transcriptional profile and regenerate tail through a process
250 transcriptionally distinct from that used by embryonic somitic mesodermal cells.
251

252 **Scalable vertebral segmentation takes place via buckling instability**

253 To understand the distinct mechanisms of vertebral segmentation during regeneration, we
254 developed a novel vertebrae extirpation assay, which uncouples vertebral segmentation from axis
255 elongation. By 1 wpi, the injury site collapsed (Fig. 6a, b). Subsequently, by 2 wpi cartilage
256 condensation was observed and the injury site expanded (Fig. 6a, b). By 3 wpi, a stereotypical
257 wrinkling pattern had formed on the outer surface of the regenerating cartilage rod (Extended Data

Fig. 9a-g). The wavelength of these wrinkles matches the wavelength of the vertebrae that form at 4 wpi (Fig. 6a, Extended Data Fig. 9a-g) Our combined observations of (i) the collapse of the injury site, and (ii) subsequent expansion of the cartilage rod and wrinkling before vertebrae patterning, suggest a buckling instability due to compression, a mechanism that has been proposed to underlie pattern formation during development of tubular structures in different organisms[22–25]. Buckling instability is a mechanics-based process of periodic pattern formation, which, unlike morphogen- or cell-based processes, is not intrinsically constrained in its scaling. This property is particularly relevant given that axolotl can regenerate their tails at all stages of their life. In this model, under weak compression or a lack of it, a rod maintains a straight and stable shape. Above a critical level of compression, stresses are relaxed locally, producing periodic surface wrinkling, with a wavelength that depends only on a few geometrical and mechanical parameters of the rod. More specifically, we developed a mechanical theory for growth in confined elastic tubes comprising a shell and a core, suggesting two regimes of wrinkling instability (See materials and methods section 'Buckling instability models' for details): i) a geometry-dominant model for tubes with very soft cores, which exhibit very little mechanical resistance to compression; in this model, the wavelength (λ , which in our theory represents the distance between vertebrae) depends only on tube geometry, scaling as $\lambda \propto R \left(\frac{h}{(1-\nu^2)^{\frac{1}{2}} R}\right)^{\frac{1}{2}}$ (λ: wavelength, R:radius, h: shell height, ν: Poisson ratio) and not on any stiffness parameters; and ii) a stiffness-dominant model for tubes with cores that have a non-negligible stiffness; in this model, the wavelength is dependent on the relative thickness of the shell and the core, scaling as $\lambda \propto h \left(\frac{E_s}{E_c}\right)^{\frac{1}{3}}$ (λ: wavelength, h: shell height, E_s: shell Young's modulus, E_c:core Young's modulus), similar to previous theories of buckling induced wrinkling during the formation of crypts and villi, and epithelial folding[25–28]. To determine

280 which model best fits vertebral segmentation during axolotl regeneration, we first measured the
281 mechanical properties of the regenerating tube, i.e., the axolotl cartilage rod, at 4 wpi, using atomic
282 force microscopy (AFM). We found that the mean Young's modulus of the core is 1.7 kPa, and
283 that of the shell is 6.9 kPa, which together demonstrate a soft core and stiffer shell (Fig. 6c, e,
284 Extended Data Fig. 9h, i). We then quantified the shell thickness (h) and tube radius (R), obtaining
285 mean values of h = 91 μm (Fig. 6f) and R = 450 μm (Extended Data Fig. 9j). Together, these
286 measurements are consistent with an intermediate regime between the two models described
287 above, with a theoretical wavelength of ~500 μm, closely matching our experimental observations
288 in a parameter-free manner (Fig. 6h, Extended Data Fig. 9g). The geometry-dominant model
289 predicts that the wavelength (λ) should increase as the cartilage rod radius (R) increases. To test
290 this we took advantage of the variable vertebrae length across the axolotl tail by recording both
291 the wavelength (λ) and the diameter for each newly formed vertebra at 3 different amputation
292 planes (4, 10, and 16 myomeres posterior to the cloaca) and used this to plot λ and radius $\sqrt{R}$. We
293 found that regardless of the amputation plane, our simple geometric prediction of $\lambda \propto \sqrt{R}$ provides
294 an excellent fit for the data (Fig. 6g, h).

295 A key prediction of the stiffness-dominant model is that altering the relative contributions
296 of the shell and core mechanics should change the vertebral wavelength (λ). To test this, we treated
297 the regenerating cartilage rod in the vertebrae extirpation assay with β-aminopropionitrile (BAPN),
298 an inhibitor of LOX-mediated collagen crosslinking[29,30]. AFM measurements at 4 wpi
299 demonstrated that the treatment with 100 μM BAPN significantly lowered the shell's Young's
300 modulus and reduced the shell thickness (Fig. 6c-f, Extended Data Fig. 9h, i), both predicting a
301 reduced wavelength, which should result in a larger number of vertebrae within a given length
302 unit. Indeed, we found that treatment with BAPN resulted in a larger number of regenerating

vertebrae compared to control in the extirpation model (Fig. 6i-k). Furthermore, during tail regeneration, transient treatment with 10 μM BAPN induced a transient reduction in the $\lambda/\sqrt{R}$ ratio, highlighting the progressive nature of buckling-instability-guided vertebrae patterning during tail regeneration (Fig. 6l, m, Extended Data Fig. 9k). Interestingly our theory assumes that external constraints from surrounding tissues prevent other modes of buckling, such as global deformation of the entire rod, which is expected under free boundary conditions. To test this, we treated the regenerating tail where one end of the rod is free with 100 μM BAPN. Strikingly, this induced global spatial oscillations of the entire rod (Fig. 6l-o) that are fully consistent with our buckling model (Fig. 6j)[31,32], and demonstrates that the cartilage rod is under a compressive load in both regeneration paradigms.

Together, these results support a quantitatively predictive buckling-instability model for vertebral segmentation during regeneration, a mechanism that inherently confers scalability to the system during regeneration (Fig. 6o).

Conclusions

Here we show that regeneration of somitic mesodermal lineages in the axolotl tail proceeds through mechanisms that are both morphologically and molecularly distinct from those that take place during embryonic development. In contrast to embryonic somitogenesis, the somitic clock gene *Hes7* plays no detectable role in vertebral segmentation during regeneration. Instead, segmentation emerges through a mechanically driven buckling instability. We identify the cellular source of regenerated somitic mesoderm as *Lfng*$^{+}$/*Meox1*$^{+}$ tenocytes, which we term Dermo-Myo-Sclero (DMS) progenitors, located at the intermyotomal space. This regenerative strategy does not closely mirror axolotl limb regeneration, where fibroblasts broadly dedifferentiate to an embryonic

326 limb-bud–like state[20,21]; rather, the tail regenerative strategy is similar to neural regeneration,
327 where defined adult stem cells undergo lineage-restricted neurogenesis[33].
328 Previous lineage-tracing studies in larval zebrafish identified a *Col1a2*-expressing connective-
329 tissue cell population capable of contributing to muscle differentiation[34,35], potentially through
330 activation of MEOX1[36]. However, because adult zebrafish do not regenerate their primary body
331 axis, the relevance of this progenitor-like state to vertebral segmentation and axial regeneration in
332 zebrafish remains unresolved.

333 Although buckling instability has not been previously proposed as a mechanism for
334 vertebral segmentation, our findings show that this model is a particularly good fit for vertebral
335 segmentation during regeneration. Specifically, because the wavelength of buckling is set by tissue
336 geometry and material properties, vertebral segmentation can automatically scale with the size and
337 growth state of the regenerating tail. This provides a robust means of generating proportionate,
338 periodic structures during large-scale tissue regeneration without reliance on a fixed molecular
339 prepattern. Such mechanically driven scaling mechanisms may represent a general strategy for
340 regenerating other large, periodic anatomical structures and warrants investigation beyond the
341 vertebral column.

342 Our findings show conceptual parallels with vertebral patterning during zebrafish
343 development[37–40]. In crown teleosts, including zebrafish, classical *Tbx18/Uncx4.1*-based
344 resegmentation is lost, and vertebral centers are specified through a mechanically mediated process
345 during which vertical myosepta transmit tension to the notochord, leading to periodic induction of
346 vertebral elements. While axolotl tail regeneration and zebrafish development employ distinct
347 molecular players, both rely on mechanical forces that reshape the tissue precursor from which the
348 vertebral column emerges. Whether this similarity reflects convergent evolution or a shared

ancestral mechanism remains unclear. Tail regeneration is widespread across Euteleostomes, spanning both Sarcopterygii and Actinopterygii. Euteleostome species capable of tail regeneration include the banded knifefish, African lungfish, the extinct early tetrapod *Microbrachis pelikani,* and lizards[41–45]. Notably, vertebral segmentation has been documented in African lungfish and in *Microbrachis pelikani*, but has not been observed in lizards[41,42,44,45].

Conceptually, our work reveals that segmented vertebrae can arise through two fundamentally distinct pathways: an embryonic, clock-based mechanism and a post-embryonic regenerative mechanism. This distinction has important implications for regenerative medicine, as it suggests that faithful reconstruction of complex axial structures may not require reactivation of embryonic programs. Instead, exploiting mechanically guided patterning of adult progenitor populations may offer an alternative and potentially more accessible route to vertebral column regeneration in other species, including humans.

Acknowledgments

We would like to acknowledge the valuable services provided by the animal facility, Molecular Biology Services, and BioOptics facilities at the IMP and IMBA; Histology, and NGS sequencing core facilities at the Vienna Biocenter; the Comparative Animal Models Core, Light Microscopy Facility (LMF; RRID:SCR_019166), and Comparative Genomics and Data Science Core at MDIBL; MDIBL receives support from the COBRE (P30GM154610) and Maine INBRE grant (P20GM103423) from NIH-NIGMS. Xenium spatial transcriptomics was carried out in the Genomics and Molecular Biology Shared Resource (RRID:SCR_021293) at Dartmouth Cancer Center, which is supported by NCI Cancer Center Support Grant 5P30CA023108 and NIH S10 (1S10OD030242) awards. We thank Dr. Stephen Sampson for proofreading this manuscript.

Competing interests

The authors declare that no competing interests exist.

Funding sources

WM is supported by an FWF Lise Meitner fellowship DOI 10.55776/M2444, project grant DOI 10.55776/P34841, and project grant DOI 10.55776/PAT4101524; TD is supported by a scholarship from the Ecole Normale Supérieure de Lyon, France; EMT is supported by an ERC AdG 742046 of the European Commission; PM is supported by grants from the NIH [NIGMS-COBRE (P20GM104318) and ORIP (R21OD031971)] and DFG-527098031.

This research was funded in whole, or in part, by the Austrian Science Fund (FWF) DOI 10.55776/M2444, 10.55776/P34841, 10.55776/PAT4101524 and the European Research Council (ERC) RegenMems 742046. For the purpose of open access, the author has applied a CC BY public copyright license to any Author Accepted Manuscript version arising from this submission.

Author contributions

Conceptualization: WM, TG, FF, EH, EMT, PM

Methodology: WM, TG, VSJ, FF, RG, RPS, MP, YST, TYL, TK, JW, JFF, FWK, JHG, EH, PM, MR, OGA, PJT, TD, GD, AA, YTS, TYL, TK, JW, EH, BT, DA

Investigation: WM, TG, VSJ, FF, RG, RPS, SCP, MP, JFF, TD, YST, TYL, TK, FWK, JHG, EH, PM, MR, OGA, TD, GD, AA, YTS, TYL, TK, JW, EH

References:

1. Rodrigo Albors, A. *et al.* Planar cell polarity-mediated induction of neural stem cell expansion during axolotl spinal cord regeneration. *eLife* **4**, e10230 (2015).
2. Cura Costa, E., Otsuki, L., Rodrigo Albors, A., Tanaka, E. M. & Chara, O. Spatiotemporal control of cell cycle acceleration during axolotl spinal cord regeneration. *eLife* **10**, e55665 (2021).
3. Poss, K. D. & Tanaka, E. M. Hallmarks of regeneration. *Cell Stem Cell* **31**, 1244–1261 (2024).
4. Cooke, J. & Zeeman, E. C. A clock and wavefront model for control of the number of repeated structures during animal morphogenesis. *J. Theor. Biol.* **58**, 455–476 (1976).
5. Baker, R. E., Schnell, S. & Maini, P. K. A clock and wavefront mechanism for somite formation. *Developmental Biology* **293**, 116–126 (2006).
6. Teillet, M. A. & Ledouarin, N. M. Consequences of Neural-Tube and Notochord Excision on the Development of the Peripheral Nervous-System in the Chick-Embryo. *Developmental Biology* **98**, 192–211 (1983).
7. Brand-Saberi, B. & Christ, B. 1 Evolution and Development of Distinct Cell Lineages Derived from Somites. in *Current Topics in Developmental Biology* vol. 48 1–42 (Elsevier, 1999).
8. Echeverri, K., Clarke, J. D. W. & Tanaka, E. M. In Vivo Imaging Indicates Muscle Fiber Dedifferentiation Is a Major Contributor to the Regenerating Tail Blastema. *Developmental Biology* **236**, 151–164 (2001).

9. Vincent, C. D., Rost, F., Masselink, W., Brusch, L. & Tanaka, E. M. Cellular dynamics underlying regeneration of appropriate segment number during axolotl tail regeneration. *BMC Dev Biol* **15**, 48 (2015).
10. Bussen, M. *et al.* The T-box transcription factor Tbx18 maintains the separation of anterior and posterior somite compartments. *Genes & Development* **18**, 1209–1221 (2004).
11. Criswell, K. E. & Gillis, J. A. Resegmentation is an ancestral feature of the gnathostome vertebral skeleton. *bioRxiv* **103**, 69–22 (2019).
12. Piekarski, N. & Olsson, L. Resegmentation in the Mexican axolotl, Ambystoma mexicanum. *J. Morphol.* **275**, 141–152 (2014).
13. Krol, A. J. *et al.* Evolutionary plasticity of segmentation clock networks. *Development* **138**, 2783–2792 (2011).
14. Bessho, Y. *et al.* Dynamic expression and essential functions of Hes7 in somite segmentation. *Genes Dev.* **15**, 2642–2647 (2001).
15. Fujimuro, T. *et al.* Hes7 3'UTR is required for somite segmentation function. *Scientific Reports* **4**, 6462 (2014).
16. Biddy, B. A. *et al.* Single-cell mapping of lineage and identity in direct reprogramming. *Nature* **564**, 219–224 (2018).
17. Kong, W. *et al.* CellTagging: combinatorial indexing to simultaneously map lineage and identity at single-cell resolution. *Nat Protoc* 1–25 (2020) doi:10.1038/s41596-019-0247-2.

18. Trobridge, G. D. Foamy virus vectors for gene transfer. *Expert Opin Biol Ther* **9**, 1427–36 (2009).

19. García-García, D. *et al*. The essential role of connective-tissue cells during axolotl limb regeneration. Preprint at https://doi.org/10.1101/2025.03.30.645595 (2025).

20. Gerber, T. *et al*. Single-cell analysis uncovers convergence of cell identities during axolotl limb regeneration. *Science (New York, N.Y.)* **362**, eaaq0681-13 (2018).

21. Lin, T.-Y. *et al*. Fibroblast dedifferentiation as a determinant of successful regeneration. *Developmental Cell* **56**, 1541-1551.e6 (2021).

22. Varner, V. D., Gleghorn, J. P., Miller, E., Radisky, D. C. & Nelson, C. M. Mechanically patterning the embryonic airway epithelium. *Proc. Natl. Acad. Sci. U.S.A.* **112**, 9230–9235 (2015).

23. Gill, H. K. *et al*. The developmental mechanics of divergent buckling patterns in the chick gut. *Proc. Natl. Acad. Sci. U.S.A.* **121**, e2310992121 (2024).

24. Shyer, A. E. *et al*. Emergent cellular self-organization and mechanosensation initiate follicle pattern in the avian skin. *Science* **357**, 811–815 (2017).

25. Hannezo, E., Prost, J. & Joanny, J.-F. Instabilities of Monolayered Epithelia: Shape and Structure of Villi and Crypts. *Phys. Rev. Lett.* **107**, 078104 (2011).

26. Hannezo, E., Prost, J. & Joanny, J.-F. Theory of epithelial sheet morphology in three dimensions. *Proc. Natl. Acad. Sci. U.S.A.* **111**, 27–32 (2014).

27. Shyer, A. E. *et al*. Villification: How the Gut Gets Its Villi. *Science* **342**, 212–218 (2013).

28. Santos-Durán, G. N., Cooper, R. L., Jahanbakhsh, E., Timin, G. & Milinkovitch, M. C. Self-organized patterning of crocodile head scales by compressive folding. *Nature* **637**, 375–383 (2025).

29. Wilmarth, K. R. & Froines, J. R. In vitro and in vivo inhibition of lysyl oxidase byaminopropionitriles. *Journal of Toxicology and Environmental Health* **37**, 411–423 (1992).

30. Makris, E. A., Responte, D. J., Paschos, N. K., Hu, J. C. & Athanasiou, K. A. Developing functional musculoskeletal tissues through hypoxia and lysyl oxidase-induced collagen cross-linking. *Proc. Natl. Acad. Sci. U.S.A.* **111**, (2014).

31. Timoshenko, S., P. & Gere, J., M. *Theory of Elastic Stability*. (McGraw-Hill, 1961).

32. Euler, L. Methodus inveniendi lineas curvas maximi minimive proprietate gaudentes sive solutio problematis isoperimetrici latissimo sensu accepti. (1744).

33. Lust, K. *et al.* Single-cell analyses of axolotl telencephalon organization, neurogenesis, and regeneration. *Science* **377**, eabp9262 (2022).

34. Ma, R. C., Jacobs, C. T., Sharma, P., Kocha, K. M. & Huang, P. Stereotypic generation of axial tenocytes from bipartite sclerotome domains in zebrafish. *PLoS Genet* **14**, e1007775 (2018).

35. Sharma, P., Ruel, T. D., Kocha, K. M., Liao, S. & Huang, P. Single cell dynamics of embryonic muscle progenitor cells in zebrafish. *Development* dev.178400 (2019) doi:10.1242/dev.178400.

36. Nguyen, P. D. *et al.* Muscle Stem Cells Undergo Extensive Clonal Drift during Tissue Growth via Meox1-Mediated Induction of G2 Cell-Cycle Arrest. *Cell Stem Cell* **21**, 107-119.e6 (2017).

37. Wopat, S. *et al.* Spine Patterning Is Guided by Segmentation of the Notochord Sheath. *CellReports* **22**, 2026–2038 (2018).

38. Wopat, S. *et al.* Notochord segmentation in zebrafish controlled by iterative mechanical signaling. *Developmental Cell* S1534580724002387 (2024) doi:10.1016/j.devcel.2024.04.013.

39. Peskin, B. *et al.* Notochordal Signals Establish Phylogenetic Identity of the Teleost Spine. *Current biology : CB* **30**, 2805-2814.e3 (2020).

40. Lleras Forero, L. *et al.* Segmentation of the zebrafish axial skeleton relies on notochord sheath cells and not on the segmentation clock. *eLife* **7**, 15–4 (2018).

41. Verissimo, K. M. *et al.* Salamander-like tail regeneration in the West African lungfish. *Proceedings of the Royal Society B: Biological Sciences* **287**, 20192939 (2020).

42. Fröbisch, N. B., Bickelmann, C. & Witzmann, F. Early evolution of limb regeneration in tetrapods: evidence from a 300-million-year-old amphibian. *Proc Biol Sci* **281**, 20141550 (2014).

43. Ellis, M. M. *The Gymnotid Eels of Tropical America*. (Published by the authority of the Board of Trustees of the Carnegie Institute, Pittsburgh :, 1913). doi:10.5962/bhl.title.43182.

44. Vonk, A. C. *et al.* Single-cell analysis of lizard blastema fibroblasts reveals phagocyte-dependent activation of Hedgehog-responsive chondrogenesis. *Nat Commun* **14**, 4489 (2023).

45. Fisher, R. E. *et al.* A Histological Comparison of the Original and Regenerated Tail in the Green Anole, *Anolis carolinensis*. *The Anatomical Record* **295**, 1609–1619 (2012).

46. Khattak, S. *et al.* Germline transgenic methods for tracking cells and testing gene function during regeneration in the axolotl. *Stem Cell Reports* **1**, 90–103 (2013).

47. Kawaguchi, A. *et al.* Chromatin states at homeoprotein loci distinguish axolotl limb segments prior to regeneration. *bioRxiv* 2022.11.14.516253 (2022) doi:10.1101/2022.11.14.516253.

48. Aulehla, A. *et al.* A β-catenin gradient links the clock and wavefront systems in mouse embryo segmentation. *Nat Cell Biol* **10**, 186–193 (2008).

49. Fei, J.-F. *et al.* Efficient gene knockin in axolotl and its use to test the role of satellite cells in limb regeneration. *Proceedings of the National Academy of Sciences of the United States of America* **114**, 12501–12506 (2017).

50. Fei, J. F. *et al.* Application and optimization of CRISPR-Cas9-mediated genome engineering in axolotl (Ambystoma mexicanum). *Nat Protoc* **13**, 2908–2943 (2018).

51. Kroll, F. *et al.* A simple and effective F0 knockout method for rapid screening of behaviour and other complex phenotypes. *eLife* **10**, e59683 (2021).

52. Riquelme-Guzmán, C. & Sandoval-Guzmán, T. Methods for Studying Appendicular Skeletal Biology in Axolotls. in *Salamanders* (eds Seifert, A. W. & Currie, J. D.) vol. 2562 155–163 (Springer US, New York, NY, 2023).

517 53. Pende, M. *et al*. A versatile depigmentation, clearing, and labeling method for exploring
518 nervous system diversity. *Sci Adv* **6**, (2020).
519 54. Kurth, T. Immunocytochemistry of the amphibian embryo--from overview to
520 ultrastructure. *Int J Dev Biol* **47**, 373–383 (2003).
521 55. Kurth, T. *et al*. Electron Microscopy of the Amphibian Model Systems Xenopus laevis
522 and Ambystoma mexicanum. in *Methods in Cell Biology* vol. 96 395–423 (Elsevier,
523 2010).
524 56. Wagner, F. *et al*. *Human Photoreceptor Cell Transplants Integrate into Human Retina*
525 *Organoids*. http://biorxiv.org/lookup/doi/10.1101/2022.08.09.500037 (2022)
526 doi:10.1101/2022.08.09.500037.
527 57. Choi, H. M. T. *et al*. Third-generation in situ hybridization chain reaction: multiplexed,
528 quantitative, sensitive, versatile, robust. *Development* **145**, dev165753 (2018).
529 58. Bensimon-Brito, A. *et al*. Revisiting in vivo staining with alizarin red S - a valuable
530 approach to analyse zebrafish skeletal mineralization during development and
531 regeneration. *BMC Dev Biol* **16**, 2 (2016).
532 59. Hutter, J. L. & Bechhoefer, J. Calibration of atomic-force microscope tips. *Review of*
533 *Scientific Instruments* **64**, 1868–1873 (1993).
534 60. Kain, L. *et al*. Calibration of colloidal probes with atomic force microscopy for
535 micromechanical assessment. *Journal of the Mechanical Behavior of Biomedical*
536 *Materials* **85**, 225–236 (2018).

537 61. Andriotis, O. G. *et al.* Nanomechanical assessment of human and murine collagen
538 fibrils via atomic force microscopy cantilever-based nanoindentation. *Journal of the*
539 *Mechanical Behavior of Biomedical Materials* **39**, 9–26 (2014).
540 62. Hannezo, E., Prost, J. & Joanny, J.-F. Mechanical Instabilities of Biological Tubes. *Phys.*
541 *Rev. Lett.* **109**, 018101 (2012).
542 63. Karam, G. N. & Gibson, L. J. Elastic buckling of cylindrical shells with elastic cores—I.
543 Analysis. *International Journal of Solids and Structures* **32**, 1259–1283 (1995).
544 64. Brangwynne, C. P. *et al.* Microtubules can bear enhanced compressive loads in living
545 cells because of lateral reinforcement. *The Journal of Cell Biology* **173**, 733–741 (2006).
546 65. Replogle, J. M. *et al.* Combinatorial single-cell CRISPR screens by direct guide RNA
547 capture and targeted sequencing. *Nat Biotechnol* **38**, 954–961 (2020).
548 66. Khattak, S. *et al.* Foamy virus for efficient gene transfer in regeneration studies. *BMC*
549 *Dev Biol* **13**, 9 (2013).
550 67. Wallace, H. & Maden, M. The cell cycle during amphibian limb regeneration. *Journal of*
551 *Cell Science* **20**, 539–547 (1976).
552 68. Schreckenberg, G. M. & Jacobson, A. G. Normal stages of development of the axolotl,
553 Ambystoma mexicanum. *Developmental Biology* **42**, 391–399 (1975).
554 69. Picelli, S. *et al.* Full-length RNA-seq from single cells using Smart-seq2. *Nat Protoc* **9**,
555 171–181 (2014).
556 70. Nowoshilow, S. *et al.* The axolotl genome and the evolution of key tissue formation
557 regulators. *Nature* 1–21 (2018) doi:10.1038/nature25458.

71. Schloissnig, S. *et al.* The giant axolotl genome uncovers the evolution, scaling, and transcriptional control of complex gene loci. *Proceedings of the National Academy of Sciences* **118**, e2017176118 (2021).

72. Dobin, A. *et al.* STAR: ultrafast universal RNA-seq aligner. *Bioinformatics* **29**, 15–21 (2013).

73. Butler, A., Hoffman, P., Smibert, P., Papalexi, E. & Satija, R. Integrating single-cell transcriptomic data across different conditions, technologies, and species. *Nat Biotechnol* **36**, 411–420 (2018).

74. Korsunsky, I. *et al.* Fast, sensitive and accurate integration of single-cell data with Harmony. *Nat Methods* **16**, 1289–1296 (2019).

75. Bergen, V., Lange, M., Peidli, S., Wolf, F. A. & Theis, F. J. Generalizing RNA velocity to transient cell states through dynamical modeling. *Nat Biotechnol* **38**, 1408–1414 (2020).

76. Wolf, F. A. *et al.* PAGA: graph abstraction reconciles clustering with trajectory inference through a topology preserving map of single cells. *Genome Biol* **20**, 59 (2019).

77. Angerer, P. *et al.* destiny: diffusion maps for large-scale single-cell data in R. *Bioinformatics* **32**, 1241–1243 (2016).

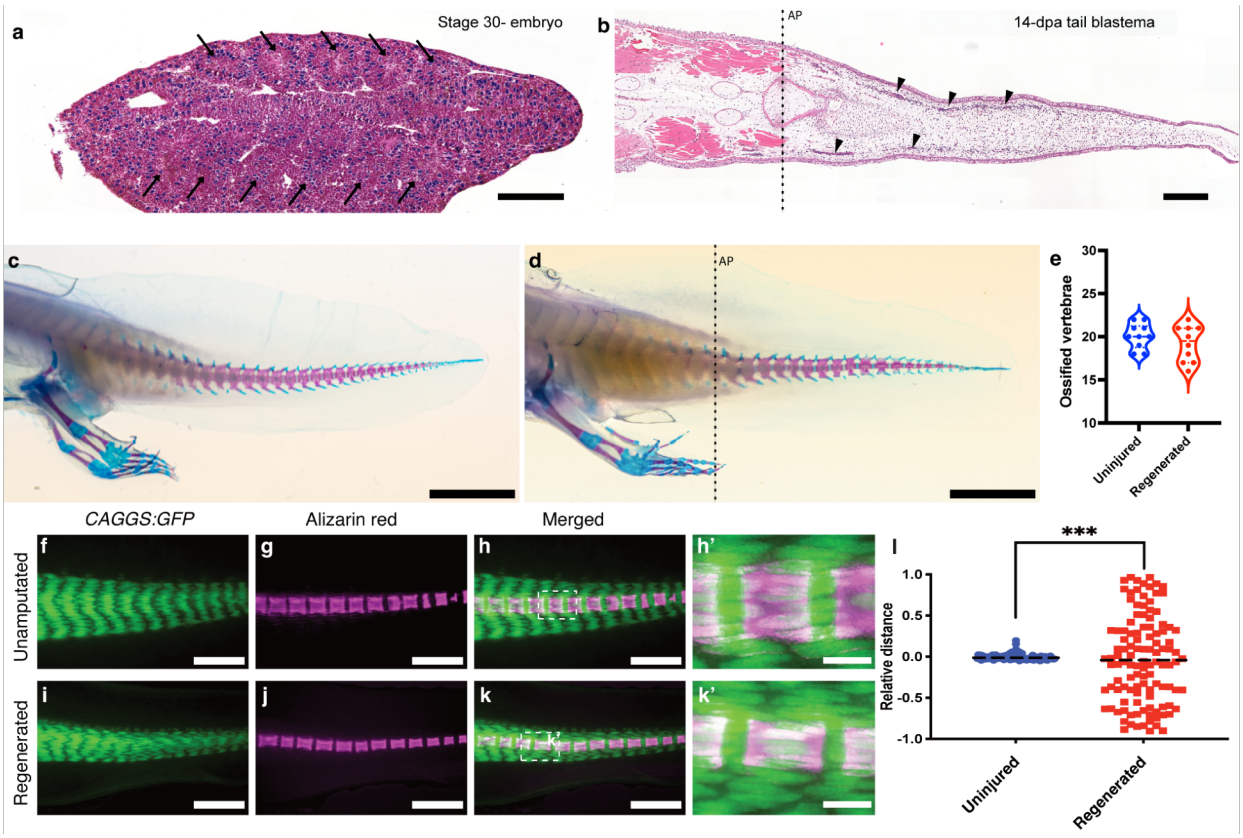

576

577 **Figure 1: Characterization of axolotl tail regeneration. a-b,** Coronal section of a H&E-stained
578 stage-30 axolotl embryo (a) and a 14-dpa tail blastema (b). Arrows indicate epithelialized somites
579 (a), and arrowheads indicate segmented myomeres (b). **c-d,** Vertebral segmentation of the
580 uninjured tail (c) is re-established in stage-matched 5-month regenerated tail (d), dashed line
581 indicates amputation plane. **e,** Quantification of ossified vertebrae numbers posterior to the cloaca
582 in uninjured (c) and stage-matched 5-month regenerated (d) animals (n= 10). **f-k**, Stereoscopic
583 images of a *CAGGS:GFP* transgenic axolotl labeled with Alizarin red S in uninjured (f-h) and
584 regenerated (i-k) tail. **l,** Quantification of muscle vertebrae off-set in the tail of h and k (n=112)
585 (off-set is calculated based on the shortest distance from the middle of a vertebra to the nearest
586 myomere boundary. Statistical analysis e: MZ-test. ns: not significant. l: F-test. ns: not significant,
587 ** $p< 0.01$, *** $p< 0.001$. Dashed lines indicate amputation plane (ap). Scale bars: a: 200 µm, b:
588 500 µm, c-d: 1 cm. f-k: 1000 µm. h', k': 200 µm.

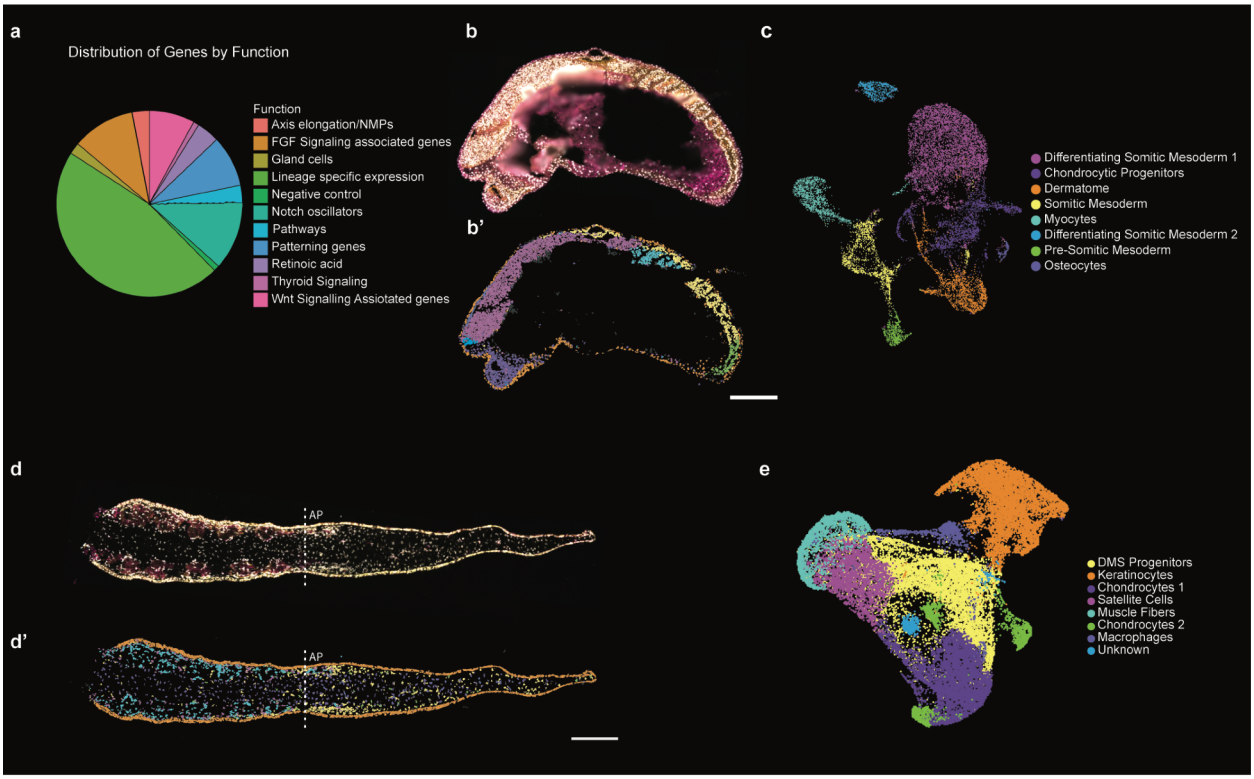
a
Distribution of Genes by Function
Function
Axis elongation/NMPs
FGF Signaling associated genes
Gland cells
Lineage specific expression
Negative control
Notch oscillators
Pathways
Patterning genes
Retinoic acid
Thyroid Signaling
Wnt Signalling Assiotated genes
b
b'
c
Differentiating Somitic Mesoderm 1
Chondrocytic Progenitors
Dermatome
Somitic Mesoderm
Myocytes
Differentiating Somitic Mesoderm 2
Pre-Somitic Mesoderm
Osteocytes
d
AP
d'
AP
e
DMS Progenitors
Keratinocytes
Chondrocytes 1
Satellite Cells
Muscle Fibers
Chondrocytes 2
Macrophages
Unknown

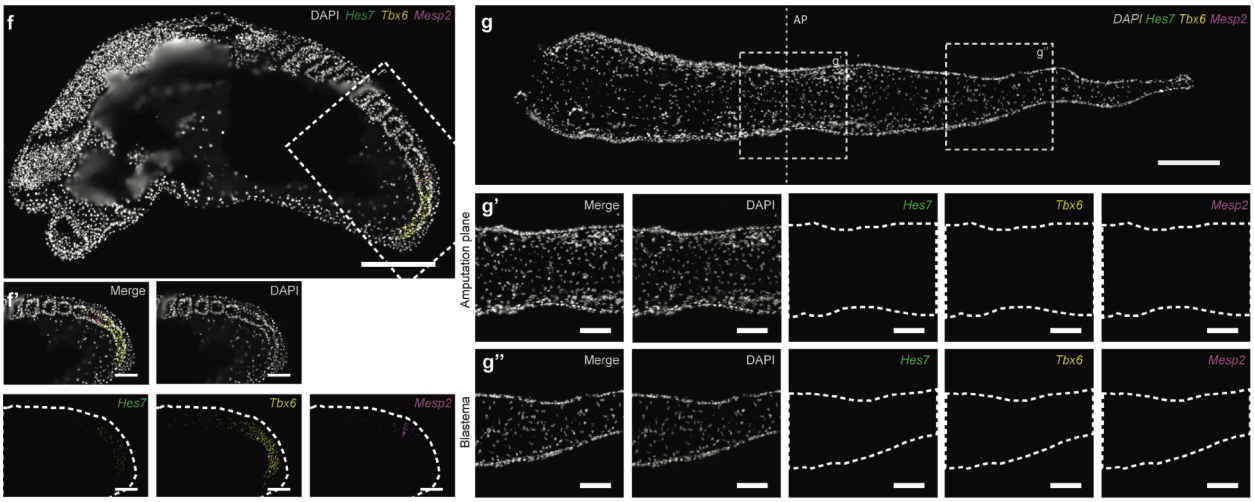
f
DAPI Hes7 Tbx6 Mesp2
f'
Merge
DAPI
Hes7
Tbx6
Mesp2
g
AP
DAPI Hes7 Tbx6 Mesp2
g'
g''
Amputation plane
Blastema
Merge
DAPI
Hes7
Tbx6
Mesp2

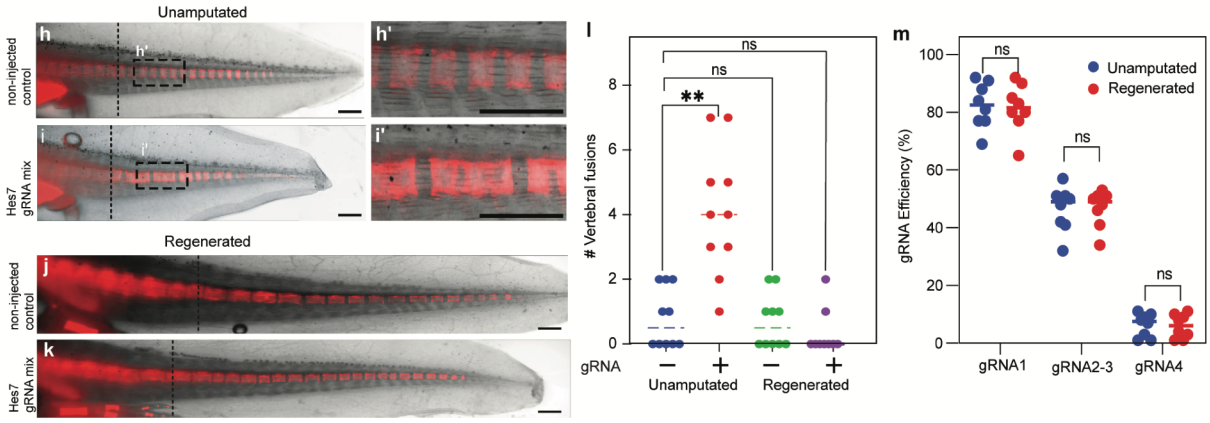
Unamputated
non-injected control
Hes7 gRNA mix
h
h'
i
i'
Regenerated
j
k
l
Vertebral fusions
ns
ns
**
gRNA
Unamputated
Regenerated
m
gRNA Efficiency (%)
Unamputated
Regenerated
ns
ns
ns
gRNA1
gRNA2-3
gRNA4

589

590 **Figure 2: Absence of key somitic clock hallmarks during axolotl tail regeneration. a,**
591 Distribution of 100 genes selected for Xenium spatial transcriptomics based on their function. **b-**
592 **c,** Analysis of a representative sagittal section from a stage-28 embryo showing histology (b),
593 spatial distribution (b'), and UMAP distribution (c) of identified cell types. **d-e,** Analysis of a
594 representative coronal section from a 2- weeks post-amputation (wpa) tail blastema showing
595 histology (d), spatial distribution (d'), and UMAP distribution (e) of identified cell types. **f-g,**
596 Xenium expression patterns for *Hes7*, *Tbx6*, and *Mesp2* in stage-28 embryo (f), and 2-wpa tail
597 blastema (g). Dashed line indicates amputation plane (ap). **h-k,** Stereoscopic images of Alizarin
598 red S labeling of segmented vertebrae in uninjured noninjected control (h), Hes7 gRNA mix-
599 injected axolotl (i), regenerated non-injected control (j), and regenerated Hes7 gRNA mix-
600 injected axolotl (k). **l,** Scoring of vertebral fusion effects in the tail (h-k) (n=10). **m,** gRNA
601 efficiency of all four Hes7 gRNAs in unamputated and regenerated tails. Statistical analysis: l:
602 Kruskal-Wallis test, followed by Dunn's test. m: one-way ANOVA, followed by Šidák
603 correction. ns: not significant, ** $p < 0.01$. Dashed lines indicate amputation plane (ap). Scale
604 bar: b, d, f-k: 500 µm. f'-g'': 200 µm.
605

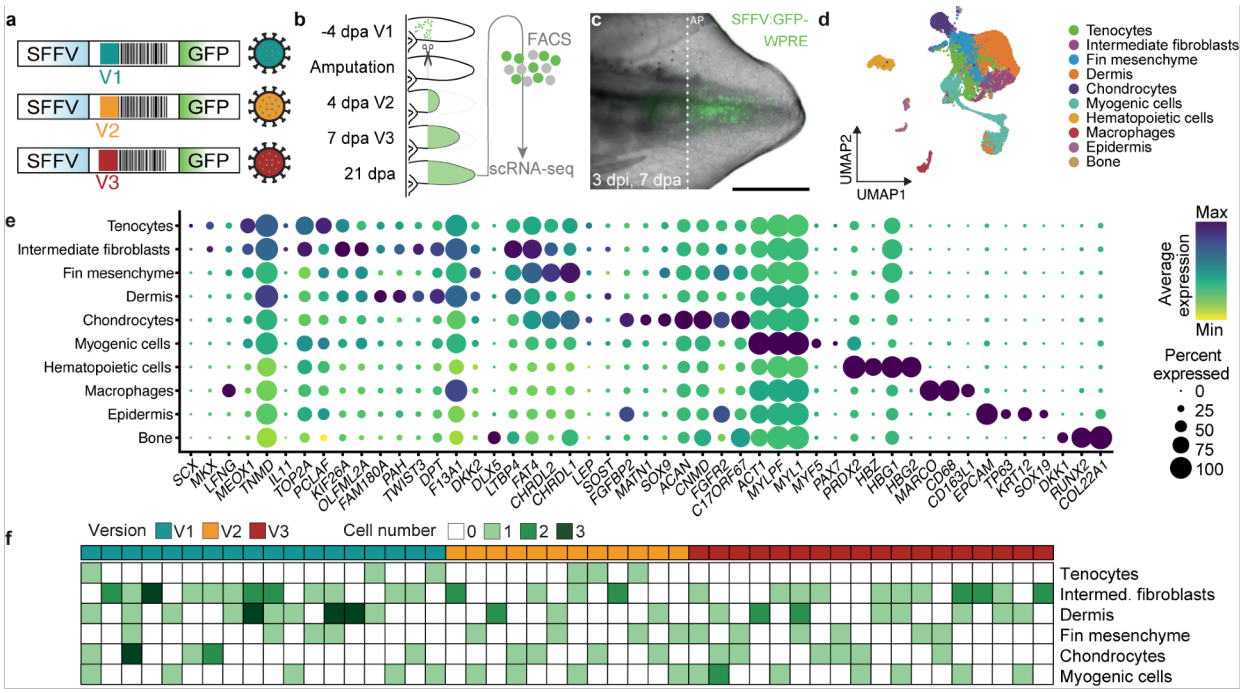

Figure 3: The axolotl tail displays a somite-like lineage potential. **a,** schematic overview of foamy virus barcode labeling vectors. **b,** Experimental overview of infection, amputation and harvesting timepoints. **c,** Representative image of a 7-dpa foamy-virus-infected axolotl tail at 3 days post infection (dpi). **d-e,** UMAP and dotplot representation of different clusters identified in GFP+ cells from foamy-virus-infected tails combining two independent replicates. **f,** Matrix-based depiction of identified clones with a Jaccard similarity index of ≥0.45 (barcodes present in ≥ 2 cells and ≥ 2 UMIs per cell). Each row represents a cell type. Each column represents a clone. Dashed lines indicate amputation plane (ap). Scale bar: c: 500 µm.

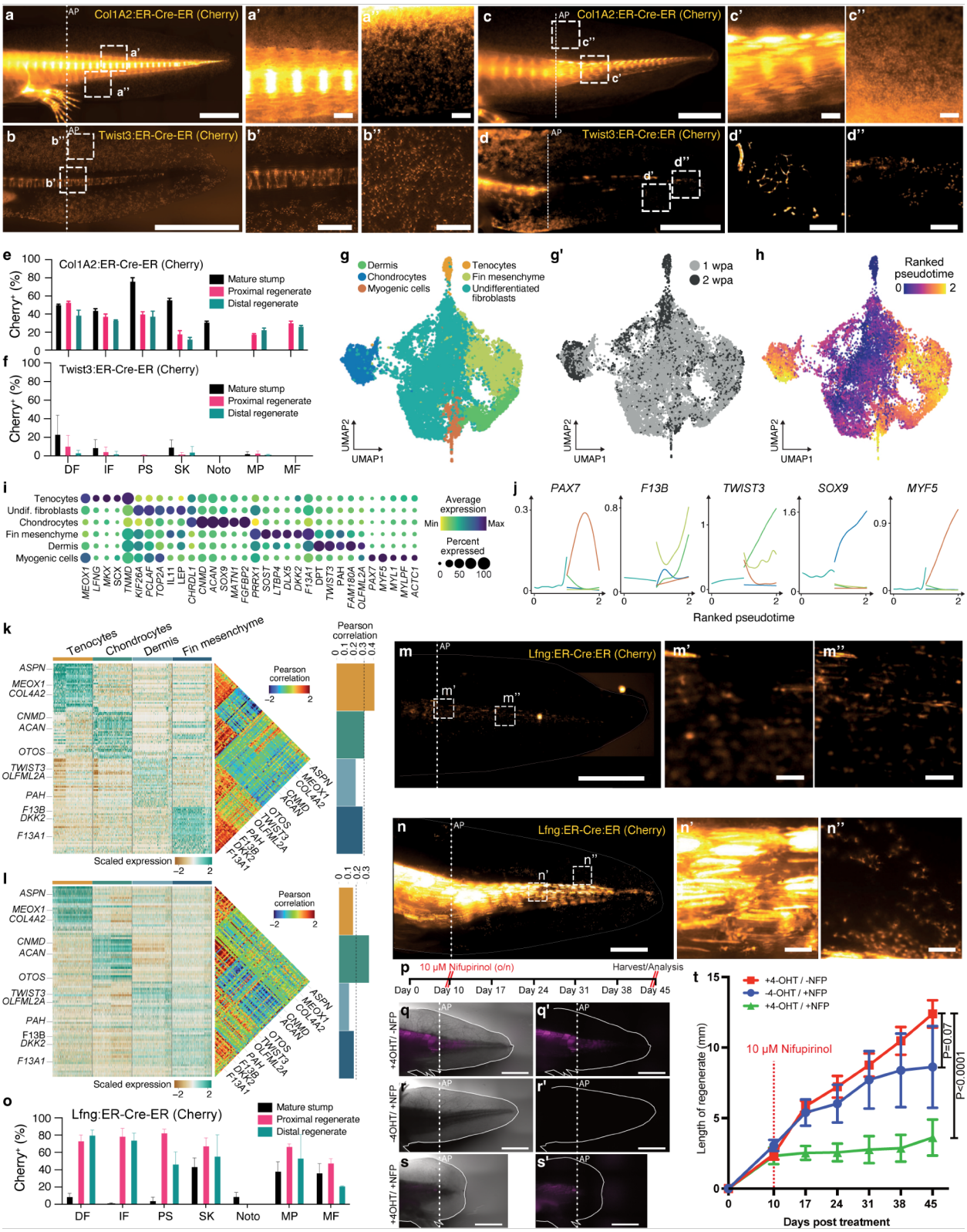
a
Col1A2:ER-Cre-ER (Cherry)
AP
a'
a''
b
Twist3:ER-Cre-ER (Cherry)
b'
b''
c
Col1A2:ER-Cre-ER (Cherry)
c'
c''
d
Twist3:ER-Cre:ER (Cherry)
d'
d''
e
Col1A2:ER-Cre-ER (Cherry)
Cherry+ (%)
Mature stump
Proximal regenerate
Distal regenerate
f
Twist3:ER-Cre-ER (Cherry)
DF
IF
PS
SK
Noto
MP
MF
g
Dermis
Chondrocytes
Myogenic cells
Tenocytes
Fin mesenchyme
Undifferentiated fibroblasts
UMAP2
UMAP1
g'
1 wpa
2 wpa
h
Ranked pseudotime
i
Tenocytes
Undif. fibroblasts
Chondrocytes
Fin mesenchyme
Dermis
Myogenic cells
MEOX1
LFNG
MKX
SCX
TNMD
KIF26A
PCLAF
TOP2A
IL11
LEP
CHRDL1
CNMD
ACAN
SOX9
MATN1
FGFBP2
PRRX1
SOST
LTBP4
DLX5
DKK2
F13A1
DPT
TWIST3
PAH
FAM180A
OLFML2A
PAX7
MYF5
MYLPF
ACTC1
Average expression
Min
Max
Percent expressed
j
PAX7
F13B
TWIST3
SOX9
MYF5
Ranked pseudotime
k
Tenocytes
Chondrocytes
Dermis
Fin mesenchyme
Pearson correlation
Scaled expression
l
m
Lfng:ER-Cre:ER (Cherry)
m'
m''
n
Lfng:ER-Cre:ER (Cherry)
n'
n''
o
Lfng:ER-Cre-ER (Cherry)
Cherry+ (%)
Mature stump
Proximal regenerate
Distal regenerate
p
10 μM Nifupirinol (o/n)
Harvest/Analysis
Day 0
Day 10
Day 17
Day 24
Day 31
Day 38
Day 45
q
q'
r
r'
s
s'
+4OHT/ -NFP
-4OHT/ +NFP
+4OHT/ +NFP
t
+4-OHT / -NFP
-4-OHT / +NFP
+4-OHT / +NFP
10 μM Nifupirinol
Length of regenerate (mm)
P=0.07
P<0.0001
Days post treatment

616

Figure 4: DMS-progenitors are necessary for tail regeneration. a-d, Labeling of 4-OHT-treated *Col1a2:ER-Cre-ER;Caggs:lp-Cherry* and *Twist3:ER-CreER;Caggs:lp-Cherry* axolotl tails before amputation (a,b), and at 6 wpa (c,d). **e,f**, Quantification of cell-type distribution at three different positions (mature stump, proximal and distal regenerate, Extended Data Fig. 3g) of the *Col1a2:ER-Cre-ER;Caggs:lp-Cherry* (e) and *Twist3:ER-CreER;Caggs:lp-Cherry* (f) regenerated tails. **g,g',** UMAP integration of cells from 7 and 14 dpa regenerated tails colored by cell-type identity (left) and by timepoint (right). **h**, Dotplot representation of cell-type marker genes (columns) across the cell type (rows) identified in g. **i**, Pseudotime estimates by a diffusion-map analysis are visualized on the UMAP embedding. **j**, Line plots represent the smoothed gene expression along their pseudotime separated by cell types. **k**,**l**, Heatmap for the top 30 markers (rows) of each cell type (columns) in the uninjured scRNA-seq data (see Extended Data Fig. 6a,b). The genes were used as input for a gene-correlation analysis visualized as a heatmap with average values within each cell type summarized as a barplot (right). Mature tail (k) and 14-dpa blastema (l) **m,n,** Labeling of 4-OHT-treated *Lfng:ER-Cre-ER;Caggs:lp-Cherry* axolotl before amputation (m) and at 6 wpa (n). **o**, Quantification of cell-type distribution of the regenerated *Lfng:ER-CreER;Caggs:lp-Cherry* tail, including the mature stump, proximal and distal regenerates. DF: dermal fibroblasts, IF: interstitial fibroblast, PS: peri-skeleton, SK: skeleton, Noto: notochord, MP: muscle progenitor, MF: muscle fiber. (Extended Data Fig. 3g). **p,** Schematic depiction of nifurpirinol cell-ablation approach. **q-s**, Tail regenerative response after nifurpirinol-based cell ablation in *Lfng:ER-Cre-ER;Caggs:lp-Cherry* transgenic axolotl. 4-OHT treatment (p, p'), and nifurpirinol treatment (q, q') alone do not affect regeneration; only when both 4-OHT and nifurpirinol treatments are combined is tail regeneration affected (r, r'). **t**,

639 Length of the regenerating tails shown in p-r. Dashed lines indicate amputation plane (AP). Scale

640 bars: a-d, p: 500 μm; a'-d'', p': 50 μm. m-n: 1,000 μm. m'-n''. 100 μm. p-s': 4,000 μm.

641

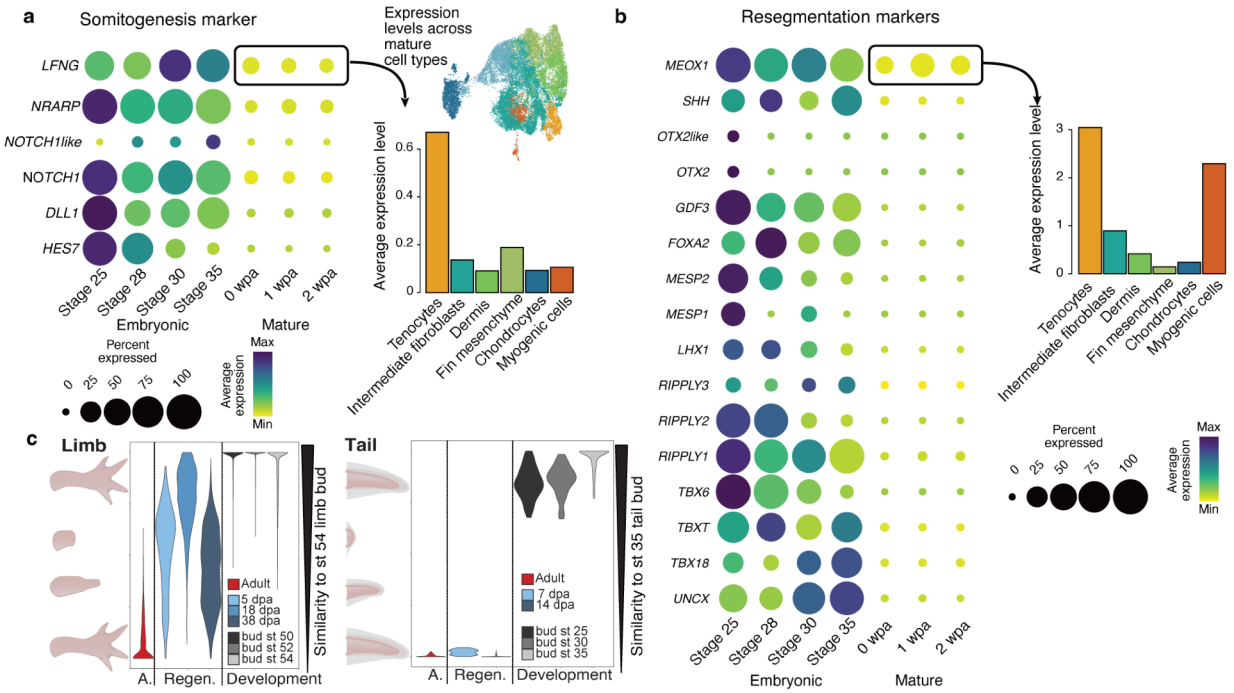

Figure 5: Tail blastema cells do not acquire a tail-bud identity during tail regeneration. a,b, Dotplot representation comparing the expression of various somitogenesis (a) and resegmentation (b) markers between tail-bud, mature-tail, and tail-blastema datasets. **c,** Comparative quadratic programming shows that limb cells acquire embryonic limb-mesenchyme identity during limb regeneration (from Lin et al.)[21] but tail cells do not acquire tail-bud identity.

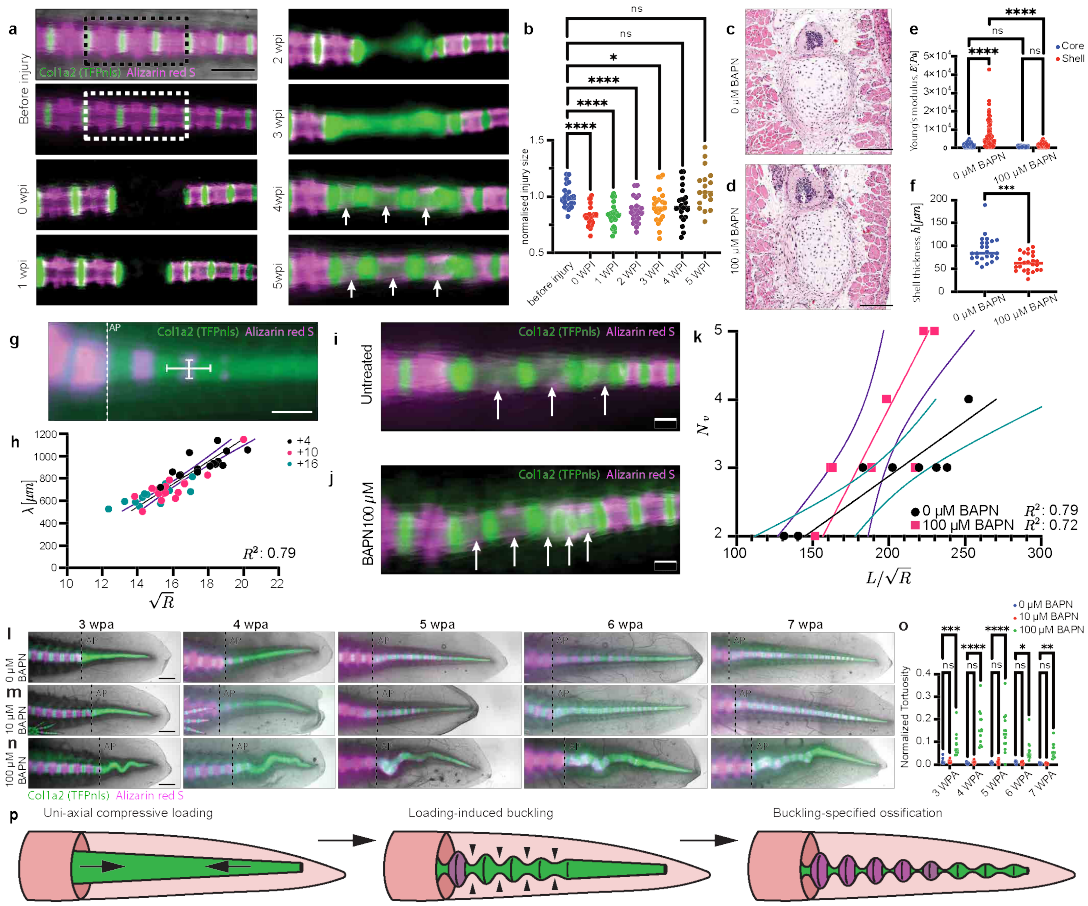

Figure 6: Vertebral segmentation during tail regeneration takes place through buckling instability. **a**, Stereoscopic images of local injury time series in *Col1a2:TFPnls* (green) axolotl labeled with Alizarin red S (magenta). Three-vertebrae injury site is marked using a dashed box. **b**, Quantification of injury-site length over a 5-week period, relative to the average injury-site length at 0 wpi. **c-d**, H&E stain of a 4-wpi cross-section after local injury untreated **(c)** and 100 μM BAPN-treated **(d)**. **e**, Young's modulus of the core and shell with and without BAPN treatment. **f**, Quantification of shell thickness with and without BAPN treatment. **g**, Stereoscopic image of *Col1a2:TFPnls* (green) axolotl labeled with Alizarin red S (magenta) at 4 wpa, depicting the recording of wavelength and diameter during tail regeneration. **h**, Quantification of λ and $\sqrt{R}$ of newly added vertebrae throughout a 7-week regenerative response. Tails were

amputated at +4, +10, and +16 myomeres posterior to the cloaca. **i-j,** Regenerated vertebrae at 5 wpi without **(i)** and with **(j)** 100 μM BAPN treatment. **k**, Quantification of the number of vertebrae at 5 wpi in the local injury relative to the aspect ratio of the regenerated cartilage rod ($L/\sqrt{R}$) **l-n**, Tail regeneration time series treated with 0 (l), 10 (m), and 100 μM BAPN (n). **o,** Normalised tortuosity of the regenerated cartilage rod in l-n, Normalised tortuosity is calculated as $\frac{Path\ length}{Euclidian\ length} - 1$. Statistical analysis: b: one-way ANOVA, followed by Šidák correction, e: two-way ANOVA, followed by Šidák correction, f: unpaired t test. h, k: simple linear fit, dashed lines indicate 95% confidence interval, o: two-way ANOVA, with Dunnett's multiple comparison. Dashed lines indicate amputation plane (ap). Arrows indicate regenerated vertebrae. Scale bar: a, g: 1,000 μm. c-d: 250 μm. i-j: 500 μm. l-n: 2,000 μm.

670 **Materials and Methods**

671 Animal husbandry, transgenesis, and 4-OH tamoxifen treatment

672 Axolotls (*Ambystoma mexicanum*) were bred in IMP and MDIBL facilities. All animal handling
673 and surgical procedures were carried out in accordance with local ethics-committee guidelines.
674 Animal experiments were performed as approved by the Magistrate of Vienna and the IACUC
675 committee of MDIBL. "White" refers to a non-transgenic *d/d* strain of axolotl that has leucistic
676 skin due to the absence of melanocytes. Animals were anaesthetized in 0.03% benzocaine (Sigma)
677 before amputation and surgery. Axolotl husbandry, transgenesis, and 4-hydroxytamoxifen (4-
678 OHT) treatment were done as previously described[43].

679 tgSceI(Mmu.*Col1a2:TFPnls-T2a-ER^{T2}-Cre-ER^{T2}*)^{Etnka}, tgSceI(*CAGGs:LoxP-GFP-LoxP-*
680 *Cherry*)^{Etnka}, tgSceI(*Caggs:LoxP-STOP-LoxP-Cherry*)^{Etnka} and tgSceI(*Caggs:Lp-BFPnls-LP-*
681 *Cherry-T2a-NTR2.0)^{Pmx}* transgenic lines are described previously[20,46,47]. To generate *Lfng*
682 transgenic animals, a mouse *Lfng*[48] driver element was cloned at the 5′ end of the GFPnls-T2A-
683 ER^{T2}-Cre-ER^{T2} (ER-Cre-ER) cassette with flanking ISceI sites. The *Twist3* transgenic animal was
684 generated by knock-in methodology described previously[49]. *Twist3* is a single-exon gene. First, to
685 generate a targeting construct, genomic sequence containing 450 bp upstream seq of the 5'UTR of
686 *Twist3* along with its 5'UTR and ORF (without stop codon) (total 1,230 bp) was amplified from
687 axolotl genomic DNA and was cloned at the 5' end of the MCS-T2a-GFPnls-T2a-ER^{T2}-Cre-ER^{T2}
688 base vector to generate 450bp_upstream_seq-5'UTR-Twist3ORF (without stop codon)-T2a-
689 GFPnls-T2a-ER^{T2}-Cre-ER^{T2} construct. Next, embryos were co-injected with the targeting
690 construct, CAS9 protein and gRNA (GCTGCAGCCCATGCAATC-TGG) with a target site 295
691 bp upstream of the ORF to create dsDNA breaks in both the genome and the targeting construct.
692 Embryos were screened for nuclear GFP fluorescence at the 3-cm stage and grown up as potential

693 breeders. Successful germ-line transmission was evaluated by nuclear GFP fluorescence in dermal
694 fibroblasts across the body, and a line was established. Constructs used for generating transgenic
695 axolotl driver lines are available at Addgene (200104, 200105, 200106, and 200107).
696
697 Xenium spatial transcriptomics
698 Axolotl embryos were staged to developmental stage 28 after fertilization and fixed overnight in
699 4% paraformaldehyde (PFA; Sigma-Aldrich, 441244-3KG) at 4°C. Embryos were washed with
700 phosphate-buffered saline (PBS) and incubated in 2% gelatin (Sigma-Aldrich, G2500-100G) at 37
701 °C in a water bath for 1 hour and placed under vacuum for 30 minutes at room temperature. The
702 embryos were washed with ice-cold PBS containing 2% gelatin, and subjected to a sucrose
703 infiltration series (7.5%, 15%, and 30%). For cryopreservation and dehydration, the embryos were
704 equilibrated in a 30% sucrose: OCT compound solution (1:1) and embedded in OCT. Samples
705 were sectioned at a thickness of 20 µm using a cryo-microtome (Leica CM1860 UV). Tails were
706 collected from animals approximately 3 cm in length that had undergone tail amputation and were
707 allowed to regenerate for 14 days. On day 14, the animals were anesthetized with 0.03%
708 benzocaine, and the regenerated tails were harvested using a scalpel (Aspen Surgical Products
709 371621). The collected tails were arranged and aligned in a cryomold containing OCT compound
710 (Leica Biosystems 14020108926). Once properly positioned, the OCT was rapidly frozen by
711 placing the cryomold on a pre-chilled heat block submerged in liquid nitrogen. Cryosections were
712 prepared at a thickness of 20 µm and subsequently transferred onto Xenium slides for downstream
713 processing. Xenium panel design, tissue histology, and processing were carried out according to
714 the manufacturer's instructions for preparing Xenium slides from fresh frozen tissues (10x
715 Genomics, Protocol: CG000579), with the following modification: slides containing embryo

samples were fixed in methanol for 2hrs at room temperature (rather than the 30min stated in the protocol). Samples were subjected to probe hybridization, ligation, and amplification steps, and stained with the Cell Segmentation Add-On Kit (10x Genomics Protocol: CG000749). Xenium slides were subsequently processed on a Xenium Analyzer instrument running Xenium Software (v.2.0.1.0) and Onboard Analysis Software (v.2.0.0.10), generating the output data bundle including principal component analysis (PCA), K-means and graph-based clustering, differential gene expression analysis, and UMAP (Uniform Manifold Approximation and Projection)-based dimensionality reduction for downstream analyses. A comprehensive list of all detected transcripts is available in GEO: GSE313338. The custom panel was designed to target 100 genes associated with somitogenesis and cell-type classification within the blastema. Each target gene was assigned 6–8 probes, designed based on the provided gene sequences. Final gene selection and probe numbers were validated by cross-referencing with unfiltered single-cell transcriptomic data to ensure balanced representation across cell types and to prevent oversaturation of any single population, which could otherwise obscure distinct fluorescent signals. Slides were stained with hematoxylin and eosin (H&E) using a Sakura Tissue-Tek Prisma stainer and imaged at 40× magnification with an Aperio GT450 scanner (Leica). Images were exported from the Xenium Browser in PNG format, corresponding to subcellular, near single-molecule RNA resolution. Exported images were imported into Fiji (ImageJ, NIH). Each image was converted to 8-bit grayscale and inverted to obtain a dark background, after which the images were binarized. Binary objects were dilated to increase dot visibility.

Xenium cell-feature matrices were processed using a custom Seurat script (version 5.3.0) to generate a combined cluster profile for the blastema and embryonic timepoints. Data were then normalized and scaled with the SC Transform package (version 0.4.2), followed by principal

739 component analysis (PCA) using all genes, with PC cutoffs of 11 and 16. The processed matrices
740 were subsequently analyzed with Find Neighbors and FindClusters, and dimensionality reduction
741 was performed with t-SNE and UMAP for visualization.
742 Xenium data were manually processed within the Xenium Explorer 3 (version 3.2.0). Sub-
743 epithelial regions of the 14-dpa blastema and embryonic tails were isolated through selections that
744 were restricted to include the blastema/pre-somitic mesoderm and a segment of uninjured/mature
745 muscle. Transcripts and cells collected in these regions were parsed using an in-house algorithm
746 developed using Python3 (version 3.10.14). Within the selection area, cells identified by Xenium
747 Ranger (version 3.1.1) were used to define sample boundaries. Boundary coordinates were
748 analyzed to orient local anatomical features, including the distal and proximal edges of the
749 tail. Xenium data are available at GSE313338.
750
751 Generation of *Hes7* mutants
752 *Hes7* mutant animals were generated by co-injecting freshly fertilized *d/d* eggs with RNP
753 complexes containing a cocktail of four different guide RNAs targeting all three exons of *Hes7*
754 using standard methods[50,51]. gRNA was prepared using primer templates and *in vitro* RNA
755 synthesis. gRNA efficiency was assessed by targeted amplification of gRNA target sites
756 compatible with Interference of CRISPR Edits (ICE) analysis. In brief, gDNA was prepared by
757 incubating 1- 2 mm of tail tissue with 200 µL of 50mM NaOH at 95°C for 15-20 minutes, and
758 subsequently neutralizing the solution by mixing it with 50 µL of 1M TRIS-in 50 mM NaOH.
759 Samples were centrifuged at 15,000 RCF for 6 minutes, and the supernatant was subsequently used
760 for PCR. 1 µL of gDNA was used to seed 50-µL PCR reactions and cleaned up for Sanger
761 sequencing using magnetic beads. Sanger sequencing was performed using a primer that is internal

762 to the amplicon. gRNA efficiency was determined through ICE analysis software (Synthego,
763 Redwood City). The following primers were used
764 sgRNA generation:
765 Common_sgRNA_reverse:
766 5'AAAAGCACCGACTCGGTGCCACTTTTTCAAGTTGATAACGGACTAGCCTTATTTTA
767 ACTTGCTATTTCTAGCTCTAAAAC 3'
768 Hes7_gRNA1: 5'
769 GAAATTAATACGACTCACTATAGGGTCGGTCAGCTTCATGGTGTTTTAGAGCTAGAA
770 ATAGC 3'
771 Hes7_gRNA2:
772 5'GAAATTAATACGACTCACTATAGGGCATGAACCACAGCCTGGGTTTTAGAGCTAG
773 AAATAGC 3'
774 Hes7_gRNA3:
775 5'GAAATTAATACGACTCACTATAGGTCAGTGGCTTCCAGAAGCGTTTTAGAGCTAG
776 AAATAGC 3'
777 Hes7_gRNA4:
778 5'GAAATTAATACGACTCACTATAGGGGGGTTCCGGAATTTCTGGTTTTAGAGCTAGA
779 AATAGC 3'
780 Sequencing:
781 Hes7_gRNA1_Fwd:5' AACTAGCTCAAACCGGCAGA 3'
782 Hes7_gRNA1_Rev:5' GAGGCCCGAACAGATATTGA 3'
783 Hes7_gRNA1_Seq:5' CTCCTGCTGGGGAAGTCAT 3'
784 Hes7_gRNA2+3_Fwd:5' TGATGCTGTTCCCGTGATAA 3'

785 Hes7_gRNA2+3_Rev:5' AGGAGGTTGGACCTCTTGGT 3'

786 Hes7_gRNA2+3_Seq:5' CACGTTGCAGGATCAGGAAT 3'

787 Hes7_gRNA4_Fwd:5' TTTCTCGCCTCACAAGGTCT 3'

788 Hes7_gRNA4_Rev:5' AAGTTCCGTTGAGGGTGATG 3'

789 Hes7_gRNA4_Seq:5' GTGGTGAGGCTGATCCATCT 3'

790

791 BAPN treatment

792 3-Aminopropionitril fumarate (Sigma-Aldrich, A3134-25G) was dissolved in tap water to generate a
793 stock solution of 100 mM, aliquoted and stored at -80 ˚C. Aliquots were further diluted into tap water
794 to reach working solutions of 10 and 100 μM. Animals were bathed in BAPN solutions and were
795 refreshed every other day.

796

797 Cell ablation using NTR2.0

798 Transgenic axolotls were generated by crossing *Lfng:GFPnls-T2A-ER^{T2}-Cre-*
799 *ER^{T2}* and *CAGGs:loxP-BFPnls-loxP-Cherry-T2a-NTR2.0* lines to enable tamoxifen-inducible
800 NTR2.0 expression in *Lfng*-positive cells. Animals (~3.5 cm, 3 months old) were housed
801 in Holtfreter's solution at 19°C under a 12-hour light/dark cycle. NTR2 expression was induced
802 by treating animals with 2 μM 4-hydroxytamoxifen (4-OHT, Sigma# H6278-50MG) via 12-hour
803 immersion on days 0, 2, and 4, followed by maintenance in 20% Holtfreter's until day
804 10, designated as 0 days post-conversion (dpc). At 0 dpc, tail amputations were performed at the
805 fifth myotome posterior to the cloaca under 0.03% benzocaine anesthesia. Animals were pre-
806 assigned into three groups: Group 1 (Nifurpirinol+, 4-OHT–, n=5) as non-converted drug-only
807 controls; Group 2 (Nifurpirinol–, 4-OHT+, n=6) as converted but no-drug controls; and Group 3

808 (Nifurpirinol+, 4-OHT+, n=7) as the ablation group targeting *Lfng*-lineage cells via NTR2-
809 mediated cytotoxicity. 10 μM Nifurpirinol (MedChem Express, HY-135470) was delivered by 24-
810 hour immersion and prepared from a DMSO stock solution. Imaging was conducted under
811 consistent conditions at 0, 10, 17, 24, 31, 38, and 45 dpc using a Zeiss AxioZoom V16 microscope
812 at 20x magnification following anesthesia in 0.03% benzocaine.
813
814 Histology
815 Embryos were fixed in Carnoy's solution, and blastema and mature tissues were fixed in 4% PFA.
816 H&E staining was done using an Epredia Gemini AS Automated Slide Stainer (Fisher Scientific,
817 Waltham) with standard protocols. Stained slides were imaged using a Panoramic 250 FLASH II
818 digital scanner (3DHistech Ltd., New Jersey).
819
820 Lineage tracing and analysis
821 To perform Cre-*Lox*P lineage tracing experiments, Cre driver lines were crossed with either
822 tgSceI(*CAGGs:LoxP-GFP-LoxP-Cherry*)^{Etnka} or tgSceI(*CAGGs:LoxP-STOP-LoxP-Cherry*)^{Etnka}.
823 Single- and double-transgenic animals were grown up to 4 cm snout-to-tail size. Animals were
824 treated three times at alternate days with 2 μM 4-OHT by bathing to obtain indelible Cherry
825 labeling of cells. Labeled animals were amputated 10 days post-conversion (from the first 4-OHT
826 treatment), near the 6th myotome from the cloaca, and contributions of *Cherry*$^{+}$ cells to the
827 regenerate were accessed by stereoscopic imaging of a regenerated tail every week for the next 6
828 weeks using an Axio Zoom.V16 (Zeiss, Jena) equipped with an Orca-Flash4.0 camera
829 (Hamamatsu Photonics, Hamamatsu) and an X-Cite Xylis LED illuminator (Excelitas

830 Technologies, Waltham). At the end of 6 weeks, tails were harvested near cloaca, and IHC or HCR
831 analysis was performed.
832
833 Antibodies
834 The primary antibodies used in these studies are rabbit anti-RFP (Rockland# 600-401-379, 1:100),
835 mouse anti-COL1A2 (DSHB # Sp1.D8, 1:100), mouse anti-PCNA (Calbiochem#NA03, 1:500),
836 mouse anti-PAX7 (DSHB#Pax7, 1:100), mouse anti-MHC (monoclonal antibody 4A1025, a kind
837 gift from S. Hughes), goat anti-SOX9 (R&D#AF3075, 1:100), rabbit anti-SOX9
838 (Chemicon#AB5535, 1:1000), rabbit anti-PRRX1[20] (1:200), and rabbit anti-Laminin (Merck,
839 #L9393 1:200). Secondary antibodies used in these studies were procured from Thermo Fisher
840 Scientific (Waltham).
841
842 Immunohistochemistry and microscopy
843 IHC staining was done as previously described[20]. Briefly, 10-µm sections were permeabilized
844 using phosphate-buffered saline (PBS) containing 0.3% Tween-20 and blocked with PBS with
845 0.3% Triton-X100 and 2% normal hose serum (Vector Laboratories # S-2000). Slides were
846 incubated O/N with primary antibodies in blocking buffer in a humidified chamber at room
847 temperature and subsequently incubated with secondary antibodies and Hoechst at a concentration
848 of 0.5 µg/mL. Mosaic images of sections were acquired on an Axio Imager.Z2 (Zeiss, Jena)
849 equipped with an Orca-Flash4.0 camera (Hamamatsu Photonics, Hamamatsu) using a 20x/0.8
850 plan-apochromat objective. Alcian blue / Alizarin red S staining was performed as previously
851 described[52]. Stained axolotls were photographed using a Nikon D40 DSLR camera with an AF-S

852 DX NIKKOR 18-55mm f/3.5-5.6G VR II objective (Nikon, Tokyo) and an iPad Air (4th gen)
853 (Apple, Cupertino) as a backlight illuminator.
854
855 Identification of different cell types based on histology
856 Collagen 1 alpha 2 (COL1A2) is an extracellular matrix (ECM) protein, and in axolotl it is
857 expressed in dermal fibroblasts and skeleton cells (28). Staining tail sections with COL1A2
858 antibodies showed broad labeling of the basal lamina (which demarcates dermal fibroblasts and
859 basal keratinocytes), skeletal and periskeletal structures, as well as fin mesenchyme. Thus, based
860 on co-staining of PRRX1 and COL1A2 along with laminin and Pax7 of sister sections, we
861 identified the following seven distinct connective-tissue subtypes (Extended Data Fig. 4): 1)
862 "Dermal fibroblasts (DF)" - cells underneath the basal lamina that are $COL1A2^{+}$ and PRRX1med;
863 2) "Interstitial fibroblasts (IF)" - cells scattered across the fin mesenchyme that are $COL1A2^{+}$ and
864 $PRRX1^{high}$ or $PRRX1^{med}$; 3) "Periskeletal cells (PS)" - cells at the periphery of skeleton that are
865 $COL1A2^{+}$ and $PRRX1^{high}$ or $PRRX1^{med}$; 4) "Skeletal cells (Sk)" - cells that reside inside
866 cartilaginous structures and are $COL1A2^{+}$ and $PRRX1^{low}$; 5) "Notochordal cells (Noto)" - large
867 vacuole-containing cells within the embryonic notochord; 6) "Muscle progenitors (MP)" - $PAX7^{+}$
868 cells scattered between muscle fibers; and 7) "Muscle fibers (MF)" - MHC^{+} or $laminin^{+}$ cells
869 within the myotome region.
870
871 Whole-mount light-sheet imaging of PCNA-labeled cells
872 In brief, axolotl samples were cleared and labeled using the Deep-Clear protocol followed by
873 imaging on a custom-built light-sheet system[53]. Samples were fixed in 4 % PFA at 4°C overnight.
874 Specimens were washed several times with PBS at room temperature to remove fixative. After

875 PBS washes, specimens were incubated in Solution-1 at 37°C for 1 day under gentle shaking. After
876 the Solution-1 treatment step of tissue clearing and five short PBS washes at room temperature,
877 samples were treated with 10 % sheep serum at room temperature for several hours. Samples were
878 then incubated with primary antibodies in 5 % sheep serum at 4°C (gentle shaking) followed by
879 additional wash steps followed by incubation with secondary antibodies in 5 % sheep serum at 4°C
880 (gentle shaking). Solution-1 consists of 8% THEED (Sigma-Aldrich, 87600-100ML), 5% Triton®
881 X 100 (Roth, 3051.2), 25% urea (Roth, X999.2) and 5% CHAPS (Hopax) in dH_2O. Solution-2
882 was prepared by mixing 50% meglumine diatrizoate (Sigma-Aldrich M5266) in PBS (pH 8.5), and
883 the refractive index was adjusted to 1.45.
884
885 Images were acquired using a custom-built light-sheet system equipped with an Olympus Plan
886 Achromat 1.0/0.25 objective (N1564200). Sample were illuminated with LightHUB 4 system
887 (Omicron, Germany) containing the following single-mode lasers: 120mW 405nm LuxX laser,
888 150mW 488nm LuxX laser, 150mW 561nm Cobalt laser, 100mW 594nm Cobalt laser, and
889 140mW 647nm LuxX laser. Images were recorded in 16-bit quality as Tiff, with a Kinetix camera
890 (Teledyne Photometrics, USA) 3200x3200px; pixel size 6.5 µm. Images were processed with
891 AMIRA (Thermo Scientific, USA) rendering software.
892
893 Immunogold labeling and electron microscopy
894 Samples were fixed in freshly prepared 4% PFA. Longitudinal 50 mm thick vibratome sections
895 were prepared on a Leica VT 1200 vibratome, and sections with target cells were selected based
896 on their Cherry fluorescence. Vibratome sections were subjected to pre-embedding immunogold
897 labeling using Nanogold and silver enhancement[54–56]. In brief, samples were blocked and

898 permeabilized in 20% normal goat serum (NGS) / PBS / 0.1% Saponin for 2 hours at room
899 temperature followed by incubation in primary antibody (rabbit anti-RFP, Rockland, # 600-401-
900 379, 1:100) in 20% NGS/0.05% saponin for 2 days at room temperature. After washes in 20%
901 NGS/0.05% saponin, the samples were incubated with goat-anti-rabbit nanogold (Fab-fragments,
902 Nanoprobes, 1:50) in 20% NGS/0.05% saponin overnight at room temperature. After final washes
903 in 20% NGS/0.05% saponin, the samples were postfixed in 1% glutaraldehyde in PBS, washed in
904 water, and silver-enhanced using the SE-Kit (Aurion, 1 hour incubation time), followed by washes
905 in water, post-fixation in 1% osmium tetraoxide/water (1 hour on ice), washes in water, *en bloc*
906 contrasting with 1% uranyl acetate (1h, on ice), washes in water, and dehydration in a graded series
907 of ethanol (30%, 50%, 70%, 90%, 96% ethanol/water, 3x 100% ethanol on a molecular sieve). The
908 samples were infiltrated in mixtures of the Epon substitute EMbed 812 with ethanol (1+2, 1+1,
909 2+1, 2x pure Epon), flat-embedded on the surface of an empty Epon dummy block, and cured
910 overnight at 65°C. The region of interest (ROI) was identified on semithin sections (1 mm) stained
911 with 1% toluidine blue/0.5% borax, and the ROI in the block was trimmed for ultrathin sectioning.
912 70-nm sections were prepared using a diamond knife (Diatome) and the Leica UC6 ultramicrotome
913 (Leica Microsystems, Wetzlar). The sections were mounted on Formvar-coated slot grids and
914 contrasted with 4% uranyl acetate/water for TEM. Finally, sections were imaged with a Jeol
915 JEM1400Plus transmission electron microscope running at 80kV acceleration voltage and
916 equipped with a Ruby digital camera (Jeol, Tokyo).
917
918 HCR-ISH
919 Samples were fixed in freshly prepared 4% PFA, prepared for cryo-sectioning, and sectioned at
920 80-µm thickness. HCR staining was performed according to the previously published protocol[57].

921 The probes were designed using probe generator software from the Monaghan lab
922 (https://probegenerator.herokuapp.com/ - the lab is no longer functional) or by the MDIBL
923 Comparative Genomics and Data Science Core team, and probes were ordered from IDT
924 (Coralville) as oligo pools. All other HCR reagents were ordered from Molecular Instruments (Los
925 Angeles).
926
927 Whole-mount HCR-FISH imaging of axolotl embryos
928 Stage-30 embryos were fixed in freshly prepared 4% PFA for 1 hour at RT. Embryos were washed
929 with PBS for 3 × 5 minutes and depigmented using 3% H_2O_2 and 0.8% KOH in DEPC-H_2O for
930 20 minutes. Next, embryos were incubated in Solution 1 of the Deep-Clear method[53] for 1 hr at
931 37°C with shaking at 500 rpm on a tabletop shaker. Embryos were washed with 5x SSC-0.1%
932 Tween-20 (SSCT) for 3 × 15 minutes at 500 rpm. Probe hybridization and amplification were done
933 according to the manufacturer's protocol (Molecular Instruments, Los Angeles). Embryos were
934 mounted in Solution-2 of the Deep-Clear protocol and incubated for 1 hr at room temperature to
935 match the refractive index before imaging. Images were acquired using a Spinning-disk confocal
936 unit (CSU-W1, 25 µm pinhole diameter, Yokogawa, Japan) on a Nikon inverted Ti-Eclipse
937 microscope stand (Nikon Instruments Inc., Japan), equipped with a Nikon CFI Plan Apochromat
938 Lambda D 10X/0.45 for whole-embryo imaging and a Nikon CFI Plan Apochromat Lambda
939 20X/0.75 lens for the cropped images. Alexa 647, Cherry and DAPI fluorescence were excited
940 with 640-nm, 561-nm, and 405-nm laser lines and collected using a 405/488/561/640 dichroic
941 beamsplitter (Yokogawa) with a ET705/72 (Chroma), ET605/52 (Chroma), and ET436/20
942 (Chroma) emission filter, respectively. Images were acquired at 2048X2048 pixels in 16 bit with
943 a Scientific CMOS Zyla 4.2 (Andor Technology, United Kingdom) controlled with NIS AR 5.41

944 (Nikon Instruments Inc., Japan) software and saved in Nd2 or Tiff file format. A maximum
945 intensity projection (MIP) of the z-stack was created using Fiji software. Images were acquired
946 using a Nikon Ti-E Yokogawa CSU-W1 / Nikon C2+ confocal microscope with a 10X Nikon CFI
947 Plan Apochromat Lambda (NA-0.45) lens for whole-embryo imaging and with a 20X Nikon CFI
948 Plan Apochromat Lambda (NA-0.75) lens for the cropped images. A MIP of the z-stack was
949 created using Fiji-ImageJ software.
950
951 Vertebrae transplantation
952 To visualize vertebrae, 5-cm *d/d* and *CAGGs:eGFP* animals were soaked in 0.05% Alizarin red S
953 (ARS) for 30-60 minutes and rinsed several times in fresh tap water[58]. Subsequently, axolotls were
954 anaesthetized in 0.03% benzocaine (Sigma) and prepared for surgery. Using a SZX16 stereo-
955 microscope (Olympus, Tokyo) equipped with a Zyla sCMOS camera (Andor, Belfast) and an X-
956 Cite Xylis LED illuminator (Excelitas Technologies, Waltham, MA) fluorescent microscope to
957 visualize vertebrae, and fine forceps, 3-4 vertebrae were carefully extirpated from the *d/d* host.
958 Subsequently, 3-4 vertebrae were dissected from the donor and grafted into the previously
959 prepared host. Axolotls were left to recover for 2 weeks, after which tails were amputated through
960 the GFP^+ donor vertebrae and lineage-traced for a total of 6 weeks.
961
962 Local injuries
963 Local injuries were performed on 4-7-cm-long *Col1a2:TFPnls-T2a-ER^{T2}-Cre-ER^{T2}* animals
964 soaked in 0.05% ARS for 30-60 minutes and rinsed several times in fresh tap water[58].
965 Subsequently, axolotls were anaesthetized in 0.03% benzocaine (Sigma) and prepared for surgery.
966 Using a SZX16 stereo-microscope (Olympus, Tokyo) equipped with a Zyla sCMOS camera

967 (Andor, Belfast) and an X-Cite Xylis LED illuminator (Excelitas Technologies, Waltham, MA)
968 fluorescent microscope to visualize vertebrae, and fine forceps, 3 vertebrae were carefully
969 extirpated at 10-15 myomeres posterior to the cloaca. To track the regenerative response, animals
970 were imaged up to 8 weeks after injury using an Axio Zoom.V16 (Zeiss, Jena) equipped with an
971 Orca-Flash4.0 camera (Hamamatsu Photonics, Hamamatsu) and an X-Cite Xylis LED illuminator
972 (Excelitas Technologies, Waltham).
973
974 Atomic force microscopy
975 Regenerated axolotl vertebrae were surgically removed on pre-chilled plates. Regenerated tissue
976 was flash-frozen in OCT on dry ice. OCT blocks were trimmed and cryo-sectioned at -10°C at a
977 thickness of 20 µm. Sections were collected on electrocharged slides and stored at -80 ˚C. Atomic
978 force microscopy (AFM) experiments were conducted on a JPK NanoWizard ULTRA SpeedA
979 (JPK-Bruker) AFM system equipped with an AXIO Observer.D1 (Zeiss) inverted optical
980 microscope. MLCT-O10 C (Bruker) tipless cantilevers, of 0.009 N/m measured spring constant
981 via the thermal noise method[59], were furnished with a borosilicate glass microsphere (SPI Supplies
982 Uniform Microspheres) 15 µm in diameter as previously described[60].
983 Immediately after removing a glass slide from the freezer, a 10-30 µl droplet of PBS was placed
984 on the cryosection to prevent it from drying. Subsequently, a fluid cell was mounted and sealed
985 with a two-component silicone (picodent twinsil, picodent, Germany), allowing all AFM
986 micromechanical analysis to be conducted on samples hydrated in 750 µL PBS. Cantilever
987 sensitivity was calibrated via a contact-based method in PBS, as previously described[60,61].
988 Deflection (volts) vs. z-displacement (µm) curves were recorded on a clean glass next to the

989 sample, over a 400 nm x 400 nm scan area with 32 px x 32 px resolution. This was repeated two
990 to three times until the deviation from the previous sensitivity was less than 1%.
991 Force curves were collected in both the rim and core (features), visible under brightfield
992 microscopy. On each of the 15 regions of interest (ROIs), 16 force curves were recorded in force
993 volume map mode within a 2 µm x 2 µm scan area at 4 px x 4 px resolution. Force curves were
994 recorded at 1.0 nN applied load (relative setpoint) and with a 2-µm z-length. Measurements were
995 conducted in 6 cryosections at 4wpi without BAPN treatment (2 animals), and 4 cryosections at
996 4wpi with BAPN treatment (3 animals). Force curves were analyzed with the Hertz model for
997 spherical indenters using a custom Matlab program available on Github
998 (https://github.com/Rufman91/ForceMapAnalysis) as previously described ([60]). A Young's
999 modulus value was obtained for every force curve. Only indentation moduli values resulting
1000 from fits with $R^2 > 0.96$ were considered for further analysis, and an average Young's modulus
1001 was calculated for each ROI.
1002
1003 Buckling instability models
1004 Buckling instabilities with well-defined length scales, and with smooth oscillations generically
1005 occur under compressive load due to a compromise between two different elastic materials. For
1006 the classical setting of a flat sheet of thickness h and Young modulus E_s, under compression and
1007 tethered to an infinitely large elastic half-plane of Young modulus E_c, simple scaling analysis
1008 considering the sheet-bending modulus $E_s h^3$ and the surrounding modulus E_c means that the
1009 wavelength of the instability must scale as $\lambda \propto h \left(\frac{E_s}{E_c}\right)^{\frac{1}{3}}$, with pre-factors depending on the exact
1010 geometry. In the case of a thin shell of thickness h much smaller than its radius of curvature R,
1011 this limit is expected to hold and predict the buckling instability. More specifically, in our setting,

we first only consider peristaltic deformations, i.e. rotationally symmetric, so that the tube displacement can be parametrized by $u_r(z)$ where r represents the radial direction and z the directional along the tube. We consider a resting state for a tube composed of a stiff shell of thickness h and Young's modulus E_s as well as a softer core of radius R and Young's modulus E_c. For all materials, we will take the Poisson ratio ν to be close to 0.5, i.e. an incompressibility assumption classical for biological materials. Interestingly, neglecting the mechanics of the core reflects a fundamental difference between cylindrical and flat geometries. Computing the elastic energy of the shell from its strain components[62,63], under the classical Foppl-Von Karman approximation, reveals that whereas compressed flat sheets buckle according to their fundamental mode (i.e. system size), the constraints of cylindrical geometry select a finite length scale for buckling, dependent on the aspect ratio of the shell $\lambda = 2\pi R\left(\frac{h}{(1-\nu^2)^{\frac{1}{2}}R}\right)^{\frac{1}{2}}$. In the regime of a very large radius, we go back to the previous result for flat sheets, dependent on the ratio of stiffness between core and shell $\lambda = 2\pi h\left(\frac{E_s}{E_c}\right)^{\frac{1}{3}}$. The relevance of each regime depends on the relative mechanics of the shell vs the core, i.e. the dimensionless ratio $\frac{E_s h}{E_c R}$. As discussed in the main text, we have computed these numbers via AFM and quantitative geometrical measurements, allowing us to quantitatively assess them. Interestingly, we find an intermediate parameter regime, with a ratio close to 1, as the core is approximately 5 times softer than the shell (E_c/E_s), but also approximately 4-5 times thicker (R/h). We thus compute the wavelength under each regime, at 4wpi, based on 8 independent measurements of the ratio R/h, taking in each case the average measured stiffness ratio (E_s/E_c). Under the geometrical regime, we find $\lambda = 505 \pm 80\ \mu m$, while under the differential stiffness regime, we find $\lambda = 502 \pm 144\ \mu m$, and thus, interestingly, we are in an intermediate parameter regime where both models make very

similar predictions regarding the wavelength. Importantly, reducing the stiffness or thickness of the shell is predicted to decrease the buckling wavelength, again in both regimes of the model, which is in agreement with the results from BAPN treatment. We also remark that in both regimes of the model, the wavelength of patterning can scale with geometric parameters, i.e. as long as R and h are larger in larger animals. As such, the wavelength of segmentation can scale with animal size based on purely mechanical considerations. This is very different from predictions of reaction-diffusion models, where additional complex regulatory mechanisms must be invoked to understand how diffusion coefficients or reaction rates change with animal size. Interestingly, we find signatures of this geometrical scaling in the data, as discussed in the main text. In particular, although measuring h systematically across different animal or rod sizes is complicated, as it requires AFM measurements to be precise with respect to the region of higher shell stiffness, we find strong correlation between wavelength λ and rod radius R in our tail regeneration model, as predicted in the model. In the local injury model, the number of vertebrae N should follow from the model $N = L/\lambda$ where L is the length of the injury. As we predict in our theory that $\lambda \propto \sqrt{R}$, we predict a scaling relationship between N and $L/\sqrt{R}$, something we observe experimentally, with an increased prefactor in BAPN treatment related to the decrease of E_s.

Finally, all models above assume axisymmetric deformations of the rod, i.e. that its overall position remains centered. This also assumes that we can neglect boundary deformations at the ends of the rod, i.e. that they are fixed. These assumptions are valid if the external mechanical constraints acting on the rod are strong. *In vivo*, strong constraints arise from the surrounding mesenchyme. In particular, in the local injury model, the remaining tissues provide strong constraints both at the ends of the regenerating region, and around it. However, in the tail

1057 amputation experiments, we hypothesized that external confinement might be much weaker, due
1058 to a free boundary condition at the tip of the tail. If we relax the assumption of axisymmetric
1059 deformations, and consider a third elastic medium surrounding the rod, of stiffness E_m, a second
1060 mode of buckling can generically occur, as observed for instance for microtubules under load[62,64]
1061 where the entire rod buckles out of plane. This is exactly what we observe in the $100\mu M$ BAPN
1062 scenario, providing additional confirmation for the hypothesis of pressure-induced buckling of
1063 the rod also operating under full tail amputation. In this case, and simplifying the rod material
1064 properties to the stiff shell, the wavelength can be written as $\lambda = 2\pi\sqrt{hR/2}\left(\frac{E_s}{E_m}\right)^{1/4}$. This
1065 suggests that for a shell stiffness of around 6kPa, one can explain the global buckling length
1066 scale (1-2mm) with realistic stiffnesses of the surrounding mesenchyme of a few hundred
1067 Pascals.
1068
1069 scRNAseq of mature and blastema tissue
1070 Tissue dissociation, and preparation for scRNAseq was performed as previously described[20]. In
1071 brief, tail tissue was dissociated in a dissociation solution (0.1 units/µL DNaseI, 35 µg/mL Liberase
1072 TM in 0.8X PBS) using fine forceps to continuously tear the tissue apart for approximately 30-40
1073 minutes. Samples were passed over a 70-µm Filcon filter (BD# 340605) and spun down at 2,000
1074 rcf for 3 minutes. Cells were carefully resuspended in 0.8X PBS and flow-sorted with a FACSAria
1075 III (BD Biosciences, Franklin Lakes) using an 85-µm nozzle into 200 µL of RLT buffer (Qiagen,
1076 RNA mini kit). Single-cell sequencing was done according to manufacturer's instructions (10x
1077 Genomics, Pleasanton, CA), with v3 chemistry used for all experiments except for library 65766,
1078 where v2 was used (Extended Data Fig. 8d). We used 5' 10x sequencing to capture viral-barcode-
1079 labeled samples with minor modifications[65]. Ten pmol of a GFP-specific reverse primer and a 10x-

specific overhang was spiked into the 5’ 10x droplet capture mix. An aliquot of the cDNA was amplified using a truseq read1 forward primer and a GFP-specific reverse primer with a nextera read2 overhang. This generated amplicons to perform targeted sequencing and was integrated with the data from the 5’ 10x single-cell transcriptome analysis.

Custom 5’ 10x primers used:

5'_10x_GFP_rev_spikein: 5’ AAGCAGTGGTATCAACGCAGAGTACTGGTGCAGATGAACTTCAGGG TC 3’

GFP_Truseq_GFP_fwd: 5’ CTACACGACGCTCTTCCGATCT 3’

GFP_nxt_GFP_rev: 5’ GTCTCGTGGGCTCGGAGATGTGTATAAGAGACAGAACAGCTCCTCGCCCTTG 3’

Viral barcode library production, infection, and clone calling

Viral barcode labeling was performed by modifying existing 3rd generation foamy virus vector systems based on the CellTag principle with modifications[16,18,66]. A 9-nt random barcode sequence and a defined 6-nt tag were cloned shortly behind the TSS of a puc2MD9-SFFV:GFP-WPRE[66] transfer vector plasmid using Gibson assembly. In brief, SFFV:GFP-WPRE plasmids were amplified in two separate fragments using primers with barcode-containing overhangs, and PCR products were DpnI-treated and purified using para-magnetic beads, and cloned using Gibson assembly. Immediately after assembly, samples were heat-shock-transformed into stellar competent cells (Takara Bio, Kusatsu). SOC outgrowth was performed for 1 hour at 37˚C, and a 5-µL aliquot was serially diluted and plated on ampicillin agar plates to estimate cloning efficiencies reaching a minimum complexity of $2*10^6$ colonies. Foamy virus was produced using Lenti-X 293T (Takara Bio, Kusatsu) generated as previously described and frozen at -80 ˚C for long-term storage[66]. Viral titers were determined by infecting HT-1080 cells with serial dilutions of previously frozen viral preps in multi-well plates. Four days later, plates were imaged using a

1106 Cell Discoverer 7 (Zeiss, Jena), and GFP^+ cells were scored to estimate viral titers. Concentrated
1107 virus was injected into either mature or blastema tissue using glass capillary needles and a PV830
1108 picopump (WPI, Sarasota, FL) using standard protocols[66]. We flow-sorted GFP^+ cells at 21 dpa in
1109 two independent experiments and performed scRNAseq using the 5' 10X platform. Barcoded GFP
1110 transcripts were recovered by adapting existing gRNA capture and direct sequencing approaches[65].
1111 Gibson PCR primers:
1112 CelltagV1_barcode_Fwd: 5'
1113 AGACTGAGTCGCCCGGGTACCGCGGGCCCGNNNNNNNNNACCGGTGGATCCACCGG
1114 TCGCCACCATG 3'
1115 CelltagV2_barcode_Fwd: 5'
1116 AGACTGAGTCGCCCGGGTACCGCGGGCCCGNNNNNNNNNCATCACGGATCCACCGG
1117 TCGCCACCATG 3'
1118 CelltagV3_barcode_Fwd: 5'
1119 AGACTGAGTCGCCCGGGTACCGCGGGCCCGNNNNNNNNNCGTACAGGATCCACCGG
1120 TCGCCACCATG 3'
1121 Celltag_Uni_Rev: 5' TACCCGGGCGACTCAGTCTGT
1122 AmpR_Fwd: 5' AATAAACCAGCCAGCCGGAA
1123 AmpR_Rev: 5' AAGTTGCAGGACCACTTCTG
1124
1125 Clonal analysis of viral barcode labeling
1126 Non-paraxial mesodermal lineages were excluded from the analysis. Barcodes were extracted and
1127 filtered (present in ≥ 2 cells and ≥ 2 UMIs per cell). Clones were called using a Jaccard similarity
1128 index of ≥ 0.45. The axolotl has a measured cell cycle ranging from 53-103 hours[9,67]. Assuming an

1129 average cell cycle time of 100 hours, tails infected with V1 4 days prior to amputation would have
1130 undergone 5.04 rounds of cell division, tails infected with V2 4 days after amputation would have
1131 undergone 4.08 rounds of division, and tails infected V3 7 days after amputation would have
1132 undergone 3.36 rounds of cell division. This corresponds to maximum clone sizes of 32.89 (V1),
1133 16.91 (V2), and 10.27 (V3). Reducing the Jaccard similarity index threshold results in unusually
1134 large clones being called, which is inconsistent with the known cell-division rate during tail
1135 regeneration.
1136
1137 Called clones are displayed in a matrix to visualize clonal diversity (Fig. 3f). Here each row
1138 represents a specific cell type, and each column represents a clone. To ensure that clones were not
1139 promiscuously called, we computationally combined the two independent replicates, and in this
1140 mixed population called clones using a Jaccard similarity index of ≥0.45. We found that 47/48
1141 clones were exclusively made up of cells originating from either replicate 1 or replicate 2, while
1142 only a single hybrid clone called was made up of 2 cells from replicate 1 and 1 cell from replicate
1143 2 (Extended Data Fig. 4i). This suggests that with a Jaccard similarity index of ≥0.45 we can
1144 reliably call clones in these data-sets and achieve a false discovery rate of 3.6%.
1145
1146 scRNAseq of embryonic tissue
1147 Axolotl embryos were staged to stage 25-35[68] and tail buds were dissected in 0.8X PBS under a
1148 SZX10 stereo-microscope (Olympus, Tokyo). Individual cells were manually collected using P20
1149 pipettes and prepared for Smart-seq2 using standard protocols in a 96-well format[69].
1150
1151 Processing and analysis of scRNAseq data

1152 The quality of the cDNA and resulting sequencing libraries were checked by Bioanalyzer (High
1153 Sensitivity DNA Kit, Agilent, 5067-4626). The libraries were sequenced using an Illumina
1154 NovaSeq PE150. Sequencing reads were mapped against the axolotl genome[70,71] using STARsolo
1155 (STAR 2.7.5a)[72], with parameters mimicking Cell Ranger's (10x Genomics) transcript-counting
1156 strategy. Fluorescent marker genes were manually added to the references. Data analysis was
1157 performed primarily via Seurat v3.1[73]. Ribosomal protein genes and pseudogenes were excluded
1158 from downstream analyses. Generally, cells with a very high or a very? low number of transcripts
1159 counts, as well as those with a high mitochondrial transcript proportion, were excluded (see exact
1160 information in Table 2). When clusters were identified to be still driven only by low RNA counts
1161 in a first screening, cells belonging to these clusters were removed. To enrich connective-tissue
1162 cells, some contaminating cell types such as epidermal cells were identified and removed after an
1163 initial screening using Seurat. Seurat's built-in scale function was used to regress out differences
1164 in nUMI and percent.mt. Scaling and PCA were always performed on all genes. UMAP was
1165 applied to the top principal components (PCs) for visualization. Data integration was performed
1166 for the blastema and the uninjured data sets using Seurat's built-in Harmony[74] function to reduce
1167 the confounding effect of different batches and samples. We performed Harmony using default
1168 parameters on the library level, 100 input PCs for blastema integration, and 50 input PCs for
1169 uninjured integration. The integration of the uninjured and blastema data sets was performed using
1170 Harmony on the library level with slightly adapted parameters (PC=50, theta=2, lambda=9).
1171

1172 Trajectory analysis

1173 To infer directionality of developmental trajectories during regeneration, we used scVelo[75]. To
1174 infer the ratio of spliced and unspliced reads using scVelo, the sequencing data were mapped with

STARsolo and its built-in 'Velocyto' mode[72] to obtain spliced and unspliced count matrices, respectively. Afterwards, scVelo was used following the standard procedure (https://scvelo.readthedocs.io/en/stable/VelocityBasics) without dynamical mapping. Fifty input PCs were used for the moments calculation to obtain the arrow velocity graph. Velocity diffusion time was calculated and used as a prior for the identification of links and directionality between the clusters by PAGA.[76] The diffusion pseudotime presented in Figure 4h was calculated using the standard diffusion map algorithm[77] in order to set the DMS cells manually to 0 and demarcate them as the starting population.

Statistical analysis

Statistical analysis was performed using a combination of PRISM (version 9.0.0), and R where appropriate. Student's t-test and ANOVA were performed using PRISM. MZ structural break test was performed in R.